Turbulent transport of sea-spray in the coastal region

Benjamin Luce, Isabelle Calmet, Boris Conan, Alexander M J van Eijk

Highlights

Turbulent transport of sea-spray in the coastal region[⋆]

Benjamin LUCE, Isabelle CALMET, Boris CONAN, Alexander M.J. Van EIJK

- Large-eddy simulation of sea-spray dispersion in a complex coastal area.
- Dynamics of marine aerosols above sea and land during a diurnal cycle.
- Influence of turbulence and stratification of the atmosphere on the vertical dispersion of aerosols.

Turbulent transport of sea-spray in the coastal region

Benjamin LUCE[a,b,1,*], Isabelle CALMET[b,2,*], Boris CONAN[b,3], Alexander M.J. Van EIJK[b,c,4]

[a] *Univ. Lille, CNRS, ONERA, Arts et Metiers Institute of Technology, Centrale Lille, UMR 9014 - LMFL, Lille, F-59000, France*
[b] *Nantes Universite, Ecole Centrale Nantes, CNRS, LHEEA, UMR 6598, Nantes, F-44000, France*
[c] *TNO DSS, The Hague, The Netherlands*

Abstract

A realistic three-dimensionnal large-eddy simulation is performed for the study of turbulent transport of sea spray aerosol in the coastal region of Le Croisic, France. A new transport model for the aerosol is implemented in the ARPS code. Simulation results are compared with field measurements, both for the mean wind field and aerosol concentration. The numerical results fit well with the observations. The mean vertical concentration profile takes an exponential shape when the data is averaged over sufficiently long timeframe, whereas the 15-minute averaged profiles vary and deviate from the theory. The transport of the aerosols is analyzed in relation to the sea-land transition and the changes in thermal stability of the atmosphere during the diurnal cycle. Turbulence is found to play an important role in the mixing of aerosols in the unstable surface layer. The turbulent vertical transport of aerosols is enhanced through convective cells over the land during the day, whereas, at night, aerosols remain trapped near the surface and are trans-

*Corresponding author
Email addresses: benjamin.luce@univ-lille.fr (Benjamin LUCE), isabelle.calmet@ec-nantes.fr (Isabelle CALMET), boris.conan@ec-nantes.fr (Boris CONAN), lex.vaneijk@tno.nl (Alexander M.J. Van EIJK)

[1] 0009-0008-0489-2014
[2] 0000-0002-4777-1510
[3] 0000-0001-8464-6551
[4] 0000-0002-0130-3260

ported over appreciable horizontal distances under quasi-neutral or stable thermal conditions.

Keywords: Sea-spray aerosol, Atmospheric boundary-layer, Coastal transition, Large-eddy simulation, WRF, ARPS

1. Introduction

Sea-spray droplets are formed by the interaction between air and water, mostly from breaking waves and related phenomena. They represent a significant mass of the atmospheric aerosols (Jaenicke, 1982; Yoon et al., 2007) and thus play a major role in the Earth's radiative budget (Mallet et al., 2003; Mulcahy et al., 2008), with direct impact on climate (Lewis and Schwartz, 2004; de Leeuw et al., 2011). On a more local scale, sea-spray is of particular importance for the air quality in coastal regions, where it mixes with anthropogenic emissions (Piazzola et al., 2016; Johansson et al., 2019; February et al., 2021).

Marine aerosols have been studied extensively (Veron, 2015). A significant amount of effort has been devoted to the marine aerosol life-cycle, resulting in a better understanding of the marine aerosol production processes (Lewis and Schwartz, 2004) and the formulation of comprehensive sea-spray source (generation) functions (Grythe et al., 2014; Bruch et al., 2021). Modeling efforts have greatly advanced our knowledge of the thermodynamic processes of the aerosols over the waves within both Eulerian (Mestayer et al., 1996; van Eijk et al., 2011) and Lagrangian (Edson and Fairall, 1994; Fairall et al., 1995; Kepert et al., 1999) frameworks, as well as their dispersion into the marine atmospheric boundary layer (Vignati et al., 1998, 2001; Tedeschi and Piazzola, 2011; Lenain and Melville, 2017), and the turbulent processes that play a role here (Peng and Richter, 2017; Richter and Chamecki, 2018).

The importance of sea-spray aerosols in atmospheric boundary layer processes and extreme meteorological events is nowadays recognized and studied by means of numerical simulations at the regional scale (Luo et al., 2019; Rizza et al., 2021), sometimes taking other species of atmospheric aerosols in account as well (Ferrari et al., 2024). At a smaller scale, the details of sea-spray transport in coastal areas remains elusive despite the need to understand the aerosol influence on the local microclimate and, consequently, on the dispersion of pollutants. This is all the more important for coastal cities, where a large proportion of the world's population lives. However, studies

aimed at understanding aerosol dispersion in coastal urban areas mainly focus on anthropogenic aerosols emitted within the urban canopy (e.g. Kim et al. (2021)). Detailed analyses of sea-spray dynamics in the coastal turbulent boundary layer are rare, mostly because they are limited to numerical approaches that suffer from the complexity of three-dimensional (3D) modeling at very different scales. Nevertheless, Liang and Yu (2016) analyzed the behavior of marine aerosols in relation to turbulence during the development of a thermal Internal Boundary Layer (IBL) in an idealized configuration of the sea-land transition.

The turbulent transport of marine aerosols towards and across the coastal transition (sea-land) is studied here by means of Large-Eddy Simulations (LES) of the Atmospheric Boundary Layer (ABL) using the Advanced Regional Prediction System (ARPS, see Xue et al. (2000)). The LES approach provides access to the instationarity of the turbulent flow and enables simulating the main turbulent processes involved in the aerosol dispersion. A marine aerosol model including the newly developped source function of Bruch et al. (2021) was implemented in the ARPS model. Following Calmet et al. (2018), regional-to-microscale nested simulations were performed to study realistic meteorologic conditions in the coastal area of Le Croisic (France).

The main objectives of this study are to:

- assess the overall simulations and aerosol model through comparisons with in-situ measurements and experimental laws;
- highlight typical behavior of marine aerosols over a full diurnal cycle above sea and land;
- explore the impact of the atmospheric thermal stability and turbulence on the sea-spray aerosol transport in a complex costal region.

In Sec. 2, we present the numerical framework, the newly developped sea-spray model, and the associated case study. Subsequently, Sec. 3 presents the verification of our model by comparison with in-situ observations of wind speed and aerosol concentrations. Finally, Sec. 4 discusses the turbulent transport of the marine aerosols in the coastal area and conclusions are provided in Sec. 5.

2. Presentation of the model and case study

2.1. Sites and experimental observations

Our aim is to simulate the transport properties of sea-spray in realistic conditions, and to verify our results against experimental data. The data is extracted from an experimental campaign that took place in 2020 at the coastal area of Le Croisic in Western France (see Fig. 1e, red dot marked C). Two optical aerosol counters (Particle Measurement Systems CSASP-100 / CSASP-200) were installed at 18 m above sea level, on the sea-facing balcony of a villa located at 20 m from the coast. The raw aerosol data provided by the two optical probes were stored every second and later resampled to create a single particle size distribution (PSD) averaged over 10 minutes. The combined spectrum of the two probes spanned a particle diameter (D) range of $0.21 - 90$ μm, distributed over 91 size bins. Aerosol concentrations were expressed as $\dfrac{\mathrm{d}N}{\mathrm{d}D}$ (in $\mu\mathrm{m}^{-1} \cdot \mathrm{m}^{-3}$). Polynomials of 1^{st} (Junge) and 5^{th} order were fitted to the resulting size distribution. These polynomials provide a better representation of the distribution by smoothing the noise of individual bin counts. At the large particle side of the spectrum, bins with less than 5 counts were considered to be statistically undersampled and excluded from the polynomials. In practice, this places the upper limit of the size distribution at approximately $10 - 20$ μm. The probes had been size-calibrated prior to the experiment by introducing particles of known uniform sizes into the scattering chamber. Unfortunately, an absolute calibration for the number of particles counted per sampled air volume was not possible.

The site was equipped with a scanning doppler LiDAR (VAISALA WindCube Scan 100S) configured to provide the radial wind speed at 6 plane position indicator (PPI) scans adjusted at different elevation angle above the sea surface with a maximum range of 2.5 km (Conan and Visich, 2024). Specifically, this set-up was built to retrieve the 15 min mean values of horizontal wind speed and direction at several heights of a virtual mast located 1.5 km offshore, south of Le Croisic (red dot marked L in Fig. 1(e)). For this article, we use wind data retrieved for 18 m, 32 m, 60 m, 123 m, 173 m and 388 m above ground level (a.g.l., for simplicity here considered equal to above mean sea level). Regional information about the wind conditions was obtained from five Meteo-France meteorological stations: CH (Chemoulin), SN (St Nazaire), NM (Noirmoutier), IDY (Ile d'Yeu) and BI (Belle Ile) (Fig. 1(c)), at heights between 10 and 20 m a.g.l. depending on the station.

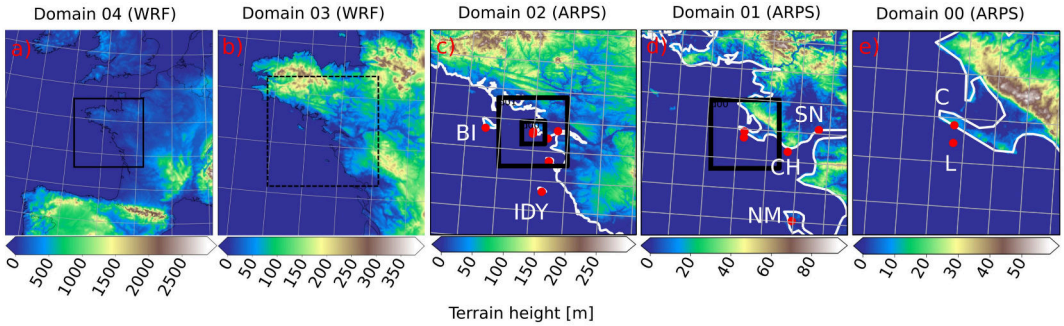

Figure 1: Domain configuration of the WRF and ARPS nested simulations with topography. Domains d04 and d03 are WRF. Domains d02, d01 and d00 are ARPS. The red dots represent locations where simulated (ARPS) data is compared to experimental observations: L (LiDAR), C (Croisic, physical position of the LiDAR and real data probes for the aerosol), CH (Chemoulin), SN (St Nazaire), NM (Noirmoutier), IDY (Ile d'Yeu) and BI (Belle Ile).

.

Our study focusses on 18 June 2020. The sunrise was at 04:14 UTC and the sunset at 20:07 UTC. The wind conditions were favorable for sea-spray generation and onshore transport, with a steady wind of 8 ± 2 m.s^{-1} near the sea surface from south-south-westerly and later westerly directions, i.e., originating from the Atlantic Ocean.

2.2. Numerical set-up for nested simulations

The Weather Research and Forecasting (WRF) model (Skamarock et al., 2021), version 4.3.2, is used in a nested framework. The simulation has been run for 3 days, from 00:15 UTC on 16 June 2020 to 23:00 UTC on 18 June 2020, in order to allow sufficient spin-up for the meteorological conditions. The two nested WRF domains d04 and d03 are shown in Fig. 1 (a,b) which depicts the topography for the successive domains. We choose to not activate the feedback feature between the smaller domain and the larger one, limiting the simulation to a one-way nested framework.

The outer domain d04 has a horizontal span $L_x = L_y = 1377$ km, while the inner domain d03 is $L_x = L_y = 459$ km large. A ratio of three is taken between the horizontal resolution of the two domains (Michioka and Chow, 2008; Bauer et al., 2020). The vertical grid is automatically stretched non-linearly to a pressure height of 50 hPa (which results in a height of

around 20 km). Both domains have the same vertical grid. They are centered on Le Croisic, using the GPS coordinates 47.278°N (latitude) and 2.518°E (longitude). Tab. 1 gives an overview of the simulation parameters. We refer to these simulations as Reynolds Average Navier-Stokes (RANS) simulations because Reynolds-averaged equations are solved using a Planetary Boundary Layer (PBL) scheme to parameterize the mean turbulent fluxes.

Table 1: Main parameters for the nested WRF simulations

Domain	d04	d03
Model	WRF/RANS	WRF/RANS
Horiz. Res. $\mathrm{d}x = \mathrm{d}y$ (m)	4500	1500
Mesh $N_x \times N_y \times N_z$	$306 \times 306 \times 80$	$307 \times 307 \times 80$
Total number of cells	7 490 880	7 539 920
Time step $\mathrm{d}t$ (s)	15	5

The WRF simulations are performed using the CONUS physics suite. The suite incorporates the soil physics (NOAH) (Niu et al., 2011) by a procedure that vertically stacks four 1-meter high cells. We used the default (most refined) soil database. An hourly forcing is imposed at the boudaries of d04 (east-west and north-south) from the ECMWF ERA5 dataset (Hersbach et al., 2020), which has a horizontal resolution $\mathrm{d}x = \mathrm{d}y = 30$ km and vertically comprises 38 pressure levels. Note that WRF only simulates the meteorological variables and that aerosols are not considered. Outputs from the smallest WRF domain d03 are saved every 15 minutes and used as forcing conditions to ARPS.

The simulations are then further refined with ARPS (Xue et al., 2000), a non-hydrostatic and compressible LES model, in which a sea-spray generation function and transport model have been implemented. A more detailled explanation on the numerical set up for ARPS and new implementations is given in the following subsections.

2.3. Numerical set-up for the ARPS model

From the results of the WRF simulations, three one-way grid nested simulations (domains d02 to d00) are successively performed with ARPS using realistic conditions. The forcing at the lateral boundaries is done using numerical data at coarser resolution. An update interval of 15 minutes between

each lateral boundary forcing is applied, as a good trade-off between the storage limit of present computers and the performance of the model (Michioka and Chow, 2008).

Table 2: Main parameters for the nested ARPS simulations. $\mathrm{d}z_{\min}$ is the minimum vertical resolution near the surface. $\mathrm{d}z$ is the mean resolution over the domain heigth.

Domain	d02	d01	d00
Model	ARPS/VLES	ARPS/LES	ARPS/LES
Horiz. Res. $\mathrm{d}x = \mathrm{d}y$ (m)	810	270	90
Vert. Res. $\mathrm{d}z_{\min}/\mathrm{d}z$ (m)	30/100	10/50	10/50
Mesh $N_x \times N_y \times N_z$	$283 \times 283 \times 61$	$283 \times 283 \times 81$	$283 \times 283 \times 81$
Total number of cells	4 885 429	6 487 209	6 487 209
Time step $\mathrm{d}t$ (s)	3	0.5	0.2

Analogous to Tab. 1, Tab. 2 presents the main simulation parameters for the three ARPS domains. The outer domain d02 has a horizontal span $L_x = L_y \approx 229$ km. According to the mesh size, the simulation on this domain can be considered a Very Large-Eddy Simulation (VLES) as suggested by Pope (2000), whereas the two innermost domains are regular LES domains. The intermediate domain d01 is $L_x = L_y \approx 76$ km large, the inner one d00 is $L_x = L_y \approx 25$ km. Again, a ratio of three is taken between the horizontal resolution of each nested domain and the three domains are centered on Le Croisic. The first change compared to WRF is the vertical resolution. The vertical grid is automatically stretched non-linearly, with an enhanced level density in the first 300 m, 100 m and 100 m above the surface to a height of around 6.1 km, 4.05 km and 4.05 km for the three domains d02, d01 and d00, repectively (see Vert. Res. in Tab. 2). The second change pertains to the smallest domain d00, where simulations are carried out over a shorter timeframe, from 20:00 UTC on 17 June 2020 to 23:00 UTC on 18 June 2020, instead of the full 3 days, due to the high computational cost.

We use a multi-layer land-surface model based on Chen and Dudhia (2001) with four 1-meter soil layers. The land-surface model computes surface fluxes from stability-dependent surface drag coefficients and predicted surface temperature, as well as surface volumetric water content. The data describing the topography (database from IGN, Institut national de l'information géographique et forestière, at 25-meters horizontal resolution), soil texture (European Soil Data Base, ESDB, at 1-kilometer horizontal resolution) and

land coverage (Corine Land Cover, CLC 2018[5], at 100-meters horizontal resolution) are extracted using the open-source geographical information system QGIS (QGIS Development Team, 2022).

We adapted the standard 13 soil types in ARPS (mostly corresponding to the USDA sand-clay-silt triangle classification) using the ESDB (Hiederer, 2013). Missing soil data, mostly due to urban coverage, is corrected with the CLC database. Details can be found in Tab. A.1 in the Appendix. The soil texture is then used by ARPS to compute heat and water exchanges through the soil layers and at the interface between the land surface and the atmosphere. Furthermore, the CLC database is used and adapted to the ARPS vegetation model. A correspondance table between the 44 classifications of the CLC and the 14 vegetation covers used in ARPS has been constructed (see Tab. A.2). This process allows to compute specific roughness lengths z_0, depending on the land cover. Finally, the Leaf Area Index (LAI), that is used in the land-surface for water and heat exchanges between the vegetation and the atmosphere, is computed from Normalized Difference Vegetation Index (NDVI) databases for the simulated period (see Appendix).

The sea surface temperature is driven by the larger WRF simulation, which is forced by the ERA5 data. In all simulations, the temperature is freely evolving between the forcing values, according to the physical laws of the model. The sea roughness length is set to a constant value of $z_0 = 0.002$ m that is several orders of magnitude lower than the land roughness lengths.

Concerning the boundary layer physics, specifically the turbulence setting for these Large-Eddy Simulations, the 1.5-order TKE subgrid-scale model of Deardorff (1980) was preferred to the Smagorinsky-Lilly first-order model also available in ARPS (Xue et al., 2000). The 1.5-TKE model has been widely used in LES modeling of the atmospheric boundary layer since the pioneering work of Moeng (1984) for resolutions ranging from a few meters to kilometers. In this model, the velocity scale required in the eddy-viscosity formulation of the subgrid-scale fluxes is determined by solving a prognostic equation for the subgrid-scale turbulent kinetic energy. The horizontal and vertical length scales used in the model are different to take into account the grid aspect ratio and the reduction of the vertical turbulent mixing in stable atmospheric conditions.

The ARPS outputs are sampled every 15 minutes, with instantaneous

[5] https://land.copernicus.eu/pan-european/corine-land-cover/clc2018

fields as well as turbulence statistics (mean, variance, etc.) performed during the last 15 minutes. The 15-minutes time intervals are chosen in accordance with Franco et al. (2019).

2.4. Sea-spray aerosol model

In the following, we detail the scalar transport model for sea-spray aerosols that was implemented in ARPS for the purpose of the study. Noting c_b the aerosol concentration for a specific bin b (which corresponds to a range of aerosol radii around a mean radius), the LES governing equation for concentration is written:

$$\frac{\partial c_b}{\partial t} + \frac{\partial \tau_{i,b}}{\partial x_i} + (u_i - v_{\text{sed},b}\delta_{i3})\frac{\partial c_b}{\partial x_i} = 0 \tag{1}$$

The index i denotes the 3 directions related to the coordinates x_i (i = 1, 2 and 3 for west-east, south-north and down-up, respectively). In Eq. 1, δ_{i3} is the Kroenecker symbol (= 1 if i = 3, 0 otherwise), u_i is the i^{th} velocity component and $v_{\text{sed},b}$ is the sedimentation velocity estimated as:

$$v_{\text{sed},b} = (\rho_{ssa} - \rho_a) g d_{ssa}^2 \frac{C_c}{18\rho_a \nu_a} \tag{2}$$

with ρ_{ssa} the sea-spray aerosol density, ρ_a the air density, g the local gravitational field of Earth, d_{ssa} the sea-spray aerosol diameter, C_c the Cunningham slip correction factor (Seinfeld and Pandis, 1998) and ν_a the air kinematic viscosity. The subgrid concentration flux $\tau_{i,b}$ is expressed as:

$$\tau_{i,b} = -K_{ssa}\frac{\partial c_b}{\partial x_i} \tag{3}$$

where K_{ssa} is the subgrid diffusivity of the sea-spray aerosols. The subgrid concentration flux (Eq. 3) follows the subgrid models implemented in ARPS, except in the first grid cell above the surface. Here $\tau_{i,b}$ is the surface flux τ_{surf} that results from the balance between the emission flux $F_{\text{emi},b}$ (non-zero only above sea surface) and the deposition flux $F_{\text{dep},b}$:

$$\tau_{\text{surf}} = F_{\text{emi},b} - F_{\text{dep},b} \tag{4}$$

The deposition flux is expressed as:

$$F_{\text{dep},b} = v_{\text{dep},b} c_b \tag{5}$$

with the deposition velocity:

$$v_{\mathrm{dep},b} = v_{\mathrm{sed},b} + \frac{1}{R_a + R_{b,b} + R_a R_{b,b} v_{\mathrm{sed},b}} \approx v_{\mathrm{sed},b} + \frac{1}{R_a} \tag{6}$$

In Eq. 6, R_a is the aerodynamic resistance in the turbulent layer that depends on the surface roughness and atmospheric stability, and $R_{b,b}$ is a quasi-laminar resistance. To a first approximation, we consider $R_a \gg R_{b,b}$, thus neglecting the brownian diffusion (as the particle radius $r_b \geq 1$ μm) and inertial impaction.

For the aerosol emission flux, $F_{\mathrm{emi},b}$, we implemented two formulations: the well-known flux model by Andreas (1998) and a more recent function by Bruch et al. (2021) that is used in this study. In this model, the aerosol flux at the sea surface is expressed by a series of lognormal modes:

$$\frac{\mathrm{d}F_{\mathrm{emi},b}}{\mathrm{d}r_{80}} = \sum_{\alpha=1}^{n=3} \frac{F_\alpha \left(\frac{u_*^3}{\nu_a g}\langle S^2\rangle\right) \tau^{-1}}{\sigma_\alpha \sqrt{2\pi}} \exp\left(-\frac{(r_{80} - \mu_\alpha)^2}{2\sigma_\alpha^2}\right) \tag{7}$$

where $\frac{\mathrm{d}F_{\mathrm{emi},b}}{\mathrm{d}r_{80}}$ is the size-dependent sea-spray generation function, r_{80} is the particule radius at the standard relative humidity of 80%, F_α is a function that depends on environmental parameters (taking into account both wave and wind characteristics), τ is the whitecap decay rate, $\langle S^2\rangle$ is the wave-slope variance, u_* is the friction velocity, μ_α and σ_α are the mean radius and standard deviation for the three considered modes. The values of F_α, μ_α and σ_α are given in Bruch et al. (2021). The whitecap decay rate τ is fixed at 3.53 s (Janssen, 1991; Varlas et al., 2021).

The wave-slope variance $\langle S^2\rangle$ cannot be derived directly in ARPS as no wave is simulated. Thus, $\langle S^2\rangle$ is estimated from the wind speed in the atmospheric surface layer (Cox and Munk, 1956):

$$\langle S^2\rangle = \frac{2}{3}\left(0.003 + 5.12 \times 10^{-3} U_{12.5} \pm 0.004\right) \tag{8}$$

where $U_{12.5}$ is the wind velocity at 12.5m above sea level. The 2/3 factor is added to extend the laboratory-based sea-spray generation function to open-ocean. The reader is referred to Bruch et al. (2023) for a detailled explanation.

Each aerosol size bin b is characterized by its center radius r_b and defined as the radius interval $r_b \in [(1 \pm 0.1) r_{80}]$. The sea-spray generation

function has been tested for different sizes and wind conditions. According to Bruch et al. (2021), the validated range is $r_{80} \in [3; 35]$ μm and $U_{10} \in [12 - 20]$ m.s^{-1}. In this paper we use the source function for slightly lower radii ($r_{80} \in \{1.0; 2.5; 5; 10; 15; 20; 25\}$ μm) and wind speeds, which is considered acceptable since Bruch et al. (2021) formulated the validity range conservatively (W. Bruch, personal communication).
Note that ARPS treats aerosols as passive scalars, which implies that no change in radius (and composition) occurs due to thermodynamic effects, coagulation or chemical reactions. Similar to the forcing scheme for the flow dynamics, the aerosol concentrations inside a domain are saved each 15 minutes and introduced in the next finer domain through lateral boundaries.

3. Model assessment with in-situ observations

3.1. Wind velocity evaluation

Table 3: Mean Bias (MB), Normalized Mean Bias (NMB) and Root Mean Square Error (RMSE) and Mean Absolute Percentage Error (MAPE)for the wind field between ARPS simulations and observations at measurement stations indicated in Fig.1c-e, on 18 June 2020.

		wind speed				wind direction	
Domain	Station (see Fig. 1)	MB [m.s^{-1}]	NMB -	RMSE [m.s^{-1}]	MAPE %	MB [deg]	RMSE [deg]
d00 (90 m)	L (18 - 33 - 60 - 123 - 173 - 388 m a.g.l)	−0.62	−0.07	1.65	15.0	−9.33	18.48
d01 (270 m)	L (18 - 33 - 60 - 123 - 173 - 388 m a.g.l)	−0.66	−0.07	1.70	15.2	−9.39	19.11
	SN (10m a.g.l.)	−1.93	−0.31	2.50	34.2	−19.61	29.35
	CH (20m a.g.l.)	−1.42	−0.16	1.91	20.0	−28.24	31.60
	NM (10m a.g.l.)	−2.20	−0.36	2.39	35.8	−17.45	21.58
d02 (810 m)	L (18 - 33 - 60 - 123 - 173 - 388 m a.g.l)	−0.63	−0.07	1.52	14.1	−9.28	18.67
	SN (10m a.g.l.)	−1.24	−0.14	2.11	33.2	−16.35	25.78
	CH (20m a.g.l.)	−1.43	−0.16	1.71	18.1	−21.82	24.94
	NM (10m a.g.l.)	−1.04	−0.16	1.31	16.8	−21.36	24.69
	IDY (10m a.g.l.)	1.72	0.46	1.91	46.4	−30.46	34.17
	BI (10m a.g.l.)	−1.59	−0.21	2.34	25.9	−18.26	22.68

The modeling of the spatio-temporal evolution of the sea-spray concentration needs several evaluation steps to ensure the reliability of the simulation.

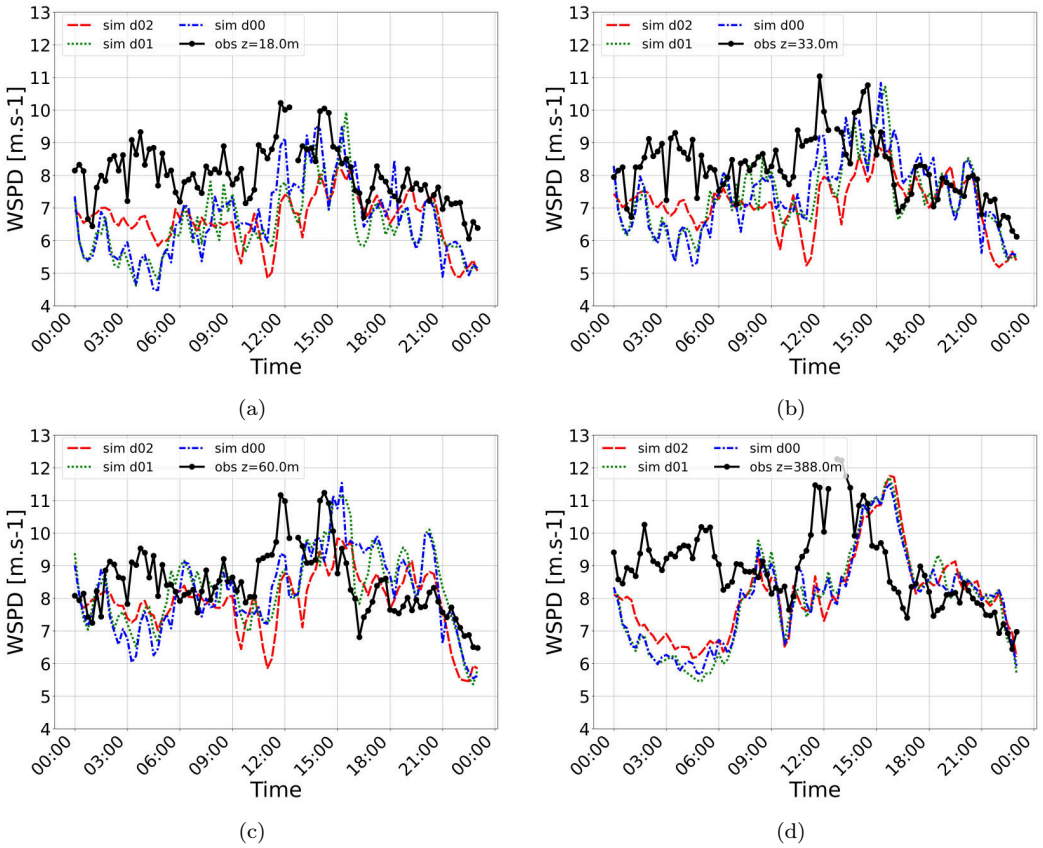

Figure 2: Time evolution [in hours] of the wind speed [in m.s^{-1}] at the LiDAR location near Le Croisic (red point L in Fig. 1) and at different altitudes a.g.l.: 18 m (a), 33 m (b), 60 m (c) and 388 m (d). The results are presented for the three ARPS nested domains, from d02 (coarsest) to d00 (finest). The black curves with dots are the observations.

.

The wind field is obviously an important factor in aerosol transport. Several on-site measurements are thus compared to the simulation results obtained with ARPS. The capability of ARPS to correctly predict the wind speed and wind direction is statistically summarized in Tab. 3. The mean bias (MB) and Root Mean Square Error (RMSE) between simulations and measurements are computed for both wind speed and wind direction, as well as the Normalized Mean Bias (NMB) and Mean Absolute Percentage Error (MAPE) for the wind speed. Upon first glance, ARPS predicts the wind field with approximately the same precision for all three domains. On close in-

spection, the agreement seems less good for domain d01 than d02, especially for the entries corresponding to the meteorological stations (cf. Sec 2.1). Furthermore, the ground-based weather stations used for comparison are located very close to the coast or on small islands (see Fig. 1) where the local wind is influenced by topographical features, whereas the LiDAR measurements are much more representative of the wind over the sea. Consequently, the better statistical scores are found for the LIDAR (average over all 6 heights), with wind speed NMBs and RMSE not exceeding 7% and 1.7 $m.s^{-1}$, respectively, and wind direction MBs of less than 10 degrees.

To gain further insight in the simulated wind field, we take advantage of LiDAR data available at various heights. The time evolution of the wind speed is presented in Fig. 2 at the LiDAR location (see Fig. 1, red point L) for different altitudes (18 m, 33 m, 60 m and 388 m a.g.l.). Both the ARPS data (sim) and LiDAR observations (obs) are averaged over 15-minutes periods. The results obtained for the three nested domains (from d02, coarsest resolution, to d00, finest resolution) are presented in each graph. The Figure shows that the model has difficulties simulating the first nighttime period (up to 06:00 UTC), but that d02 approaches the measurements better than d01 and d00. On the contrary, these two inner domains perform better than d02 from 06:00 UTC onwards, especially near the surface (Fig. 2(a-c)). Furthermore, the three individual domains yield more and more identical results at higher elevations (Fig. 2(d)).

Fig. 2 shows that the overall underestimation of the wind speed simulated with ARPS at the LiDAR location mainly results from the first night (before 06:00 UTC). During this period, the measured wind speed varies little with the altitude. On the other hand, the simulated wind speed clearly increases from 18 m to 60 m a.g.l. while lower values are simulated above (388 m a.g.l.). This suggests that ARPS predicts a different wind vertical gradient than the one measured by the LiDAR. The best agreement between nighttime simulations and observations is found at the 33 m and 60 m levels (Fig. 2(b,c)), and worsens for lower and higher altitudes (Fig. 2(a,d)). For the rest of the day (from 06:00 to 23:00 UTC), the agreement between simulations and observations is fairly good, although the simulations capture the wind speed peak in the early afternoon with a time lag which is greater at the 388 m level (Fig. 2(d)) than below. This delay could be explained by the forcing conditions, since at this height we can assume that synoptic conditions prevail over surface influence.

The discrepancies in wind speed during the first nighttime period can have several causes. One of these is an underestimation of the wind aloft, which would be influenced in the wind closer to the surface. This explanation is supported by the fact that the wind speed at 388 m a.g.l is very close for all three domains and that, as previously mentioned, the wind above the atmospheric surface layer is much more governed by the synoptic wind than by turbulent transfers near the surface. Another explanation is the possible difference in atmospheric thermal stability between observations and simulations, and between high- and low-resolution simulations. Although no information on the thermal stability of the atmosphere is available from measurements, a mean wind that varies little with height is consistent with an unstable atmosphere. In contrast, our simulations predict a stable atmosphere during the first nighttime period, with a stronger positive gradient of the potential temperature (not shown here) in d01 and d00 than in d02. The stable stratification of the atmosphere can be attributed to an underestimation sea surface temperature in the simulations. This, combined with the finer vertical resolution that enhances the heat transfer between the surface and the atmosphere, may explain the larger discrepancies in wind speed for the d01 and d00 simulations.

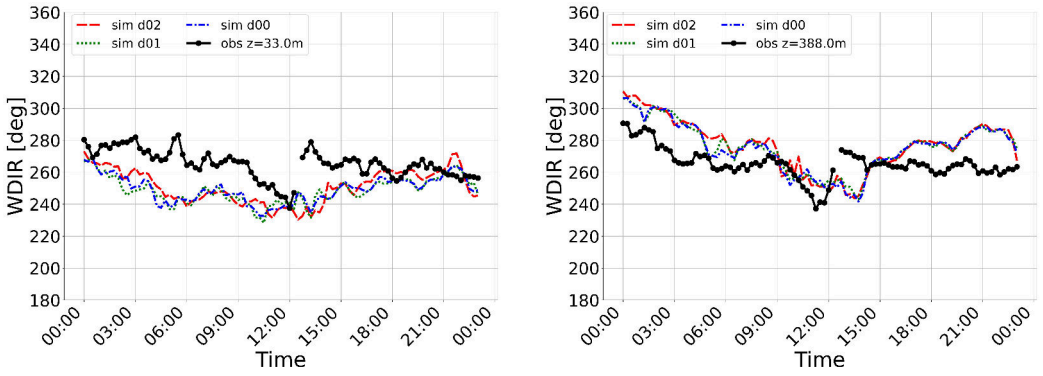

(a) (b)

Figure 3: Time evolution [in hours] of the wind direction [in degrees] at the LiDAR location near Le Croisic (red point L in Fig. 1) and at two altitudes a.g.l.: 33 m (a) and 388 m (b). The results are presented for the three ARPS nested domains, from d02 (coarsest) to d00 (finest). The black curves with dots are the observations.

Moving forward, Fig. 3 shows the time evolution of the wind direction.

The figure shows a comparison between the LiDAR measurements and ARPS simulations for two altitudes, 33 m and 388 m a.g.l., and for data that was averaged over 15-minutes timeframes. The wind direction is relatively well simulated by ARPS for the higher altitude, less well close to the surface. The best agreement is actually obtained between 100 m and 200 m a.g.l. (not shown here) but the simulations miss the sudden change in direction around 12:00 UTC (with at best a 2h delay as depicted in Fig. 3b). In addition, we note a stronger wind rotation with increasing altitude in the simulations compared to the observations, especially during the nighttime period (before 06:00 UTC). This is typical of a stable boundary layer being present at that time in the simulations, as discussed above.

Table 4: Mean Bias (MB), Normalized Mean Bias (NMB), Root Mean Square Error (RMSE) and Mean Absolute Percentage Error (MAPE) for the wind field between ARPS and the LiDAR observations for two different timeframes, on 18 June 2020.

Domain	Station (see Fig. 1)		wind speed				wind direction	
			MB	NMB	RMSE	MAPE	MB	RMSE
			[m.s^{-1}]	-	[m.s^{-1}]	%	[deg]	[deg]
d00 (90 m)	L	00:00-06:00	−1.81	−0.2	2.28	21.9	−10.66	21.56
		06:00-23:00	−0.18	−0.02	1.33	12.4	−8.94	17.23
d01 (270 m)	L	00:00-06:00	−1.72	−0.19	2.28	21.3	−11.28	22.51
		06:00-23:00	−0.27	−0.03	1.43	13.1	−8.80	17.74
d02 (810 m)	L	00:00-06:00	−1.15	−0.13	1.66	15.9	−9.26	19.49
		06:00-23:00	−0.43	−0.05	1.46	13.3	−9.40	18.44

The performance difference between daytime and nighttime prompted us to recalculate the statistical scores for the two individual timeframes. Tab. 4 shows the results, presented as an average over the 6 LiDAR heights. A comparison with Tab. 3 reveals that all scores have improved during daytime, yielding an impressive 0.18 m.s^{-1} and 9 degrees MB for wind speed and wind direction in d00, respectively. In addition, we now observe a gradual improvement of the scores when the mesh is refined, as expected. This is an important feature for the study of the transport of marine aerosols by turbulence. Consequently, we will restrict our turbulence study (Sec. 4) to the daytime (06:00 - 23:00 UTC).

As a general view over this part, we consider a wind speed difference of less than 20% (MAPE) a rather good agreement considering the simplicity of the model, compared to the complex reality of the coastal area. For the

wind direction, a difference of a few degrees is less important at the open ocean than near the coastline, where the topography influences the wind field differently depending on the wind direction. In view of the above, we do not expect our model to be a predictive tool for a detailed analysis of aerosol dispersion in the coastal zone, but rather to provide insight on the general behavior of aerosol on a typical summer day.

3.2. Sea-spray evaluation

For this step, we will compare the simulated concentration to those measured at Le Croisic (see Fig. 1), which is a delicate process for various reasons. First, it is difficult to measure instantaneous absolute concentrations of atmospheric aerosols, and even similar measurement instruments may differ by an order of magnitude (Reid et al., 2006; Veron, 2015). Furthermore, the aerosol probes used at Le Croisic classify particles according to their size, but not by chemical composition. Thus, other particles in addition to sea spray may have been sampled. Finally, the sea-spray generation function used in ARPS does not account for the surf zone at the sea-land interface, which may generate additional sea spray due to wave dissipation (van Eijk et al., 2011; Tedeshi et al., 2017). Unfortunately, this contribution is difficult to estimate: Van Eijk formulated his surf function for a upward sloping beach, whereas the coast at Le Croisic is rocky. Furthermore, the aerosol probes were located some 20 meters away from the coast line and at a height of 18 m above the waterline. It is not evident how many surf-generated aerosols actually reached the samplers.

Therefore, we will not only compare simulation results to experimental data, but also to the predictions of a parametric aerosol model providing a ballpark estimate of the sea-spray concentration, i.e., the Advanced Navy Aerosol Model (ANAM, van Eijk et al. (2011)). To this end, ANAM (version 4, without surf contribution) was used to generate a particle size distribution at 18 m above sea level for a relative humidity of 80%, and instantaneous (local) and 24h-averaged (fetch effect) wind speeds equal to 6 $m.s^{-1}$. These values correspond to the average conditions at the LiDAR site over the whole day. Fig. 4 shows the ANAM aerosol concentration as a function of particle radius (red curve) and compares it to the concentrations measured by the aerosol probes at Le Croisic (solid blue dots), revealing a remarkably good agreement. Tentatively, we conclude that the airmass sampled by the aerosol probes was predominantly marine in nature, without additional contributions from the surf zone. Fig. 4 also shows the sea-spray concentrations obtained

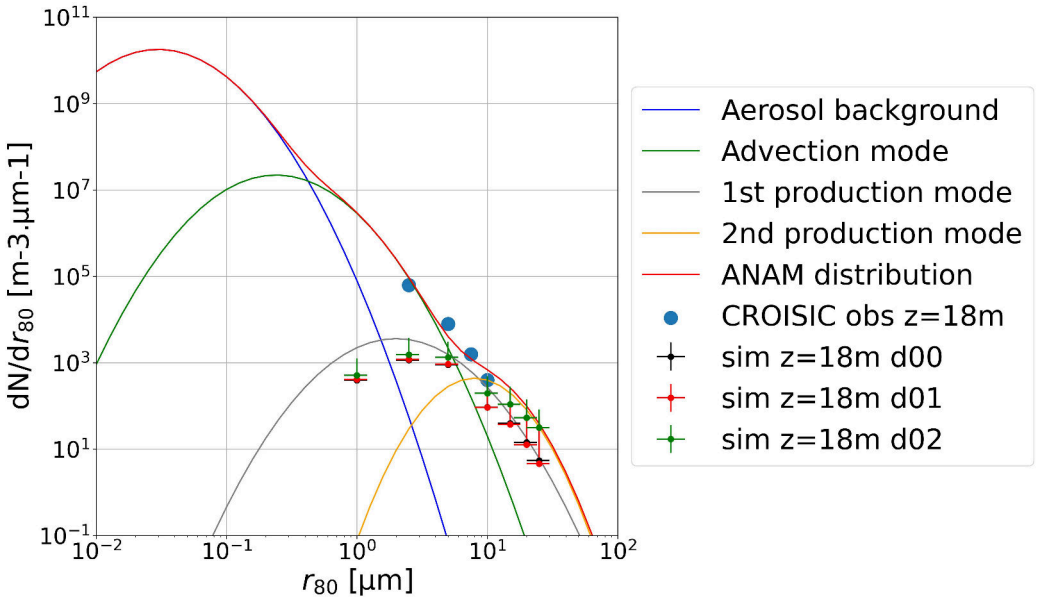

Figure 4: Aerosol concentrations measured by the PMS probes (blue dots), simulated by ARPS (crosses) and predicted by ANAM (red curve). Aerosol background and the three modes contributing to ANAM distribution are also shown.

with ARPS. The ARPS concentrations are a day-average over the individual ARPS outputs, each representative for a 15-minutes timeframe. The ARPS data are extracted at 18 m a.g.l. at the LiDAR location (L). Overall, we observe a good agreement between the ARPS concentrations, the experimental concentrations and the ANAM prediction, for radii larger than 5 μm.

For smaller radii, the ARPS concentrations drop below the measurements and ANAM, but interestingly, the ARPS concentrations at 1 μm and 2.5 μm are in good agreement with the (bi-modal) ANAM production mode. One explanation for this behavior is that ARPS simulates freshly produced sea-spray particles, but the (aged) aerosols advected over longer distances that are represented in ANAM by the advection mode (green curve in Fig. 4) are not taken into account, nor is the background concentration of aerosols. The discrepancy may also result from an underestimation of the sea-spray production at these smaller radii, which are outside the model's range of validity of $[3; 35]$ μm (Bruch et al., 2021).

For all radii, but more clearly for large aerosols, a higher concentration is observed for the low-resolution domain (d02) than for the other two do-

mains. Tentatively, we attribute this to a vertical grid effect. In the d02 domain, deposition and emission fluxes are concentrated in the first grid cell above the surface, which is at the same altitude as measurements. In the high-resolution domains (d01 and d00), there are several vertical grid cells between the surface and the 18 m level at which the measurements were made. Consequently, the concentration at the measurement height is the result of emission and deposition processes, but also of the more complex process of vertical mixing that acts to lift the aerosols to this level.

On a general note, we are quite satisfied with the comparison between ARPS, ANAM and experimental data and we consider the ARPS sea-spray generation mode successfully validated. However, if ARPS is to be used in a later stage to predict atmospheric sea-spray concentrations over a wide range of radii and over longer offshore distances, additional processes such as long time and/or distance advection and aging need to be taken into account.

To continue the validation of the sea-spray model, we plot the vertical concentration profiles for several radii in Fig. 5. The three domains are horizontally ordered from coarsest to finest, and the three radii in increasing order from top to bottom. The blue lines are the day-averaged vertical profiles of aerosol concentration as simulated with ARPS at the LiDAR location (L in Fig. 1). We fit to the ARPS data two typical profile functions, defined as:

$$N_z = N_{10} \left(\frac{z}{10} \right)^{-s_p} \tag{9}$$

for the power law (noted pow) model (Rouse, 1937; Prandtl, 1952) and:

$$N_z = N_{10} \exp \left(-s_e \frac{z}{10} \right) \tag{10}$$

for the exponential law (noted exp) model (Toba, 1965; de Leeuw, 1989), with z the height above the sea surface, N_{10} the concentration at 10 m, s_p and s_e constants. The fits are shown in Fig. 5 by the green and red lines for power and exponential functions, respectively. The constants were fixed for each radius using the results obtained in domain d00. It is evident that the ARPS profile is much better described by the exponential function, and we note a close agreement with ARPS for the d01 and d00 simulations.

Upon close inspection of Fig. 5, we observe that the value of s_e varies little over the different radii (except for the largest radius $r_b = 20$ μm not shown here). The values of s_p, in the range $0.41 - 0.54$ depending on the aerosol

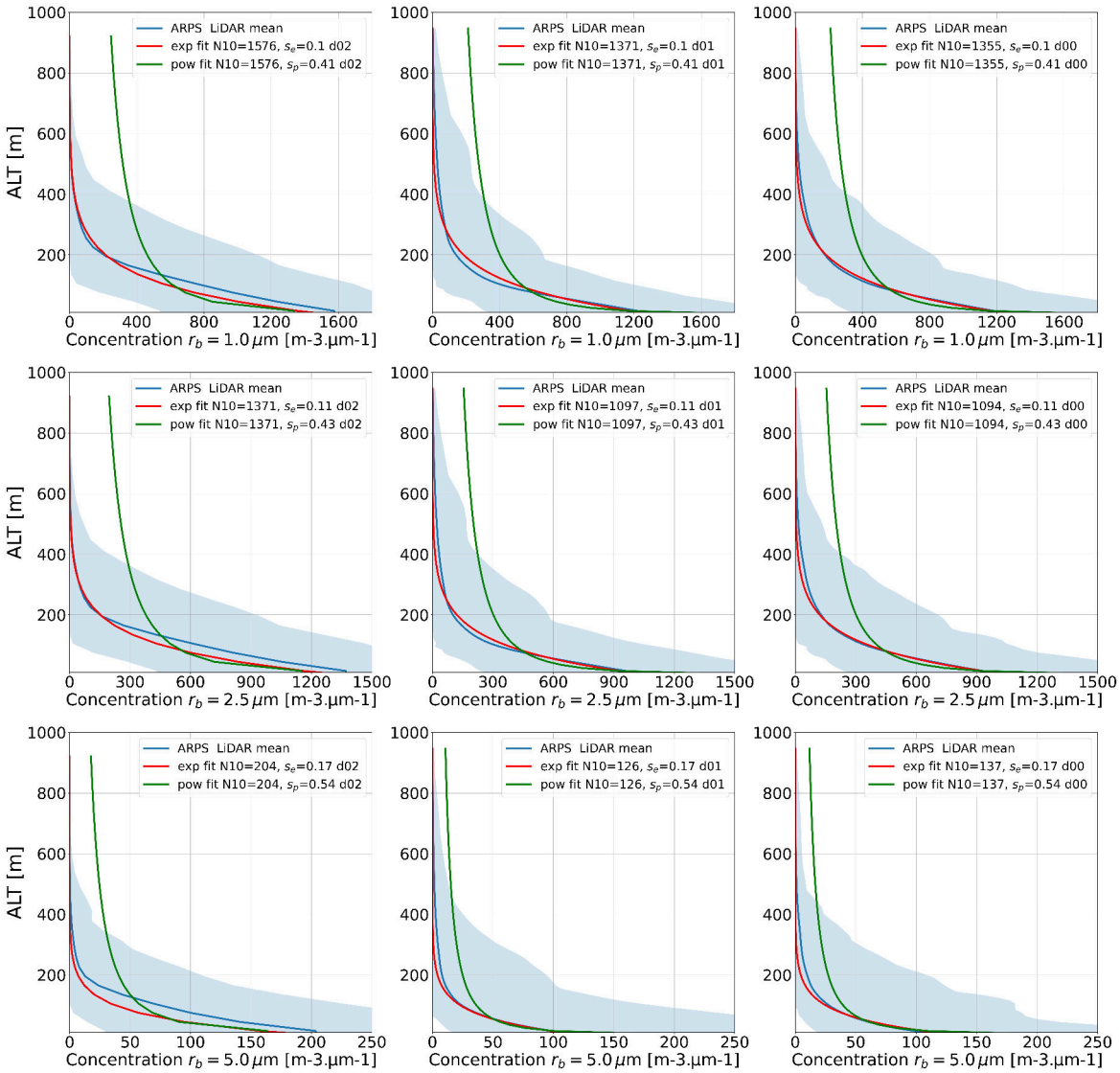

Figure 5: Vertical sea-spray concentration profiles at location L (Fig. 1). From left to right are the different domains (from d02 to d00). Each row is for a specific radius (from 1.0 μm to 5.0 μm). The blue line is the ARPS simulation, averaged over the whole day, while the blue area shows the min and max concentration during the day (taken as a 15-minutes average). The green line follows the power law (Eq. 9), the red line follows the exponential law (Eq. 10).

radius, differ from the value of 0.75 previously obtained using a combination of in-situ and satellite data (Piazzola et al., 2015), but remain in a good order of magnitude. While this suggests that the day-averages can be well described by a single function, this is not the case for individual data along the day. This is illustrated by the blue shaded area delimited by the minimum and maximum of the 15-minutes averaged concentration profiles, showing that the deviation from either theoretical model is quite large.

Summarizing our evaluation of the marine aerosols model in ARPS, we conclude that the simulations achieve a correct behavior both in sea-spray concentrations near the sea surface and in the shape of the vertical profile, at least over large time scales. However, we have noted that over a 15-minutes time average, the vertical profiles differ from either theoritical model. This observation leads us to the next part of our study: the influence of turbulence on sea-spray transport.

4. On the role of turbulence for the sea-spray transport

In the following section, the statistics of each variable are taken over 15-minutes periods starting at the time specified in the text. Some common notations are used, such as the east-west, south-north and vertical velocities (u, v and w, respectively), and we introduce the Reynolds decomposition for each instantaneous variable x:

$$x = \bar{x} + x' \tag{11}$$

where $\bar{x}$ is the time average of the variable x and x' its fluctuating part. We note the standard deviation of x as σ_x such that $\sigma_x^2 = \overline{x'^2}$, and the covariance of x and y as $\overline{x'y'}$. In our analysis, we will consider the Turbulent Kinetic Energy (TKE) $\bar{k}$, defined as:

$$\bar{k} = \frac{1}{2}\left(\sigma_u^2 + \sigma_v^2 + \sigma_w^2\right) \tag{12}$$

as well as the turbulent vertical flux of the concentration $\overline{c'w'}$.

4.1. Sea-spray concentrations in the coastal area of Le Croisic

On 18 June 2020, the airmass reaching Le Croisic originates from the sea, which implies the presence of sea-spray aerosols above the land. The wind conditions were rather constant, with only small variations in magnitude and

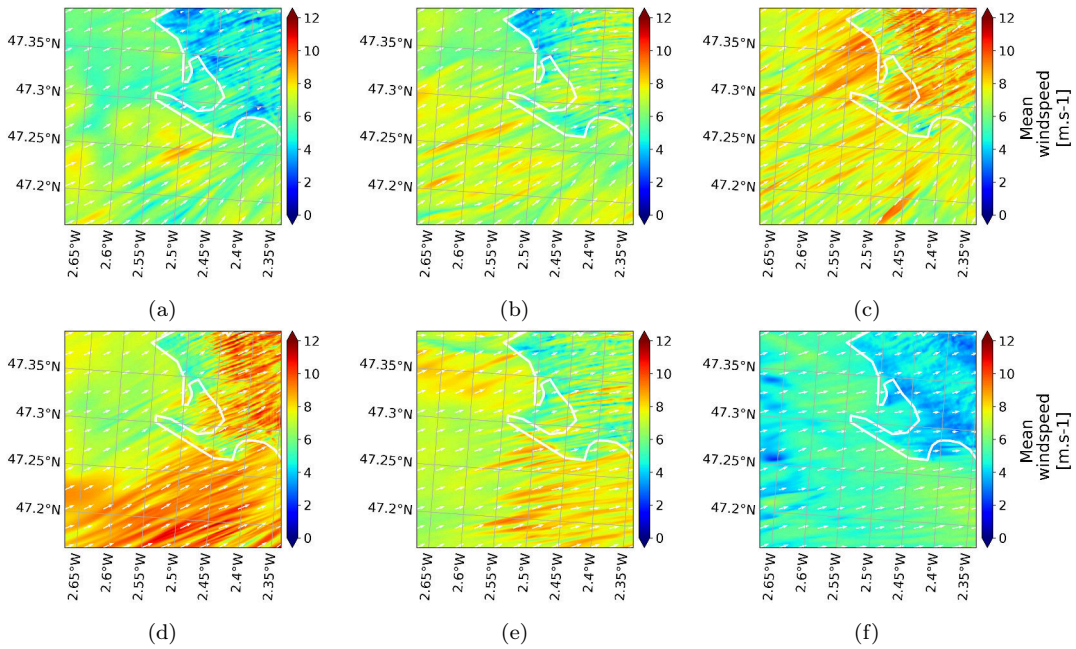

Figure 6: Averaged wind field at 20 m a.g.l. for the innermost ARPS domain d00 on 18 June 2020 at: 06:00 UTC (a), 08:00 UTC (b), 12:00 UTC (c), 14:00 UTC (d), 18:00 UTC (e) and 22:00 UTC (f). The white vectors indicate the wind direction and the colours represent the wind speed.

direction (mostly west to south-west). As an illustration, Fig. 6 shows the wind speed and direction in domain d00 at 20 m a.g.l. at six timestamps over the day. Just after sunrise, at 06:00 UTC (Fig. 6(a)), the wind is coming from the south-west, with a speed of around 6 m.s^{-1}. In the morning, the wind speed increases slightly and continues to do so (Fig. 6(b,c)). The wind is at its strongest at 14:00 UTC (Fig. 6(d)), mostly above 10 m.s^{-1}. Later in the afternoon, the wind direction is close to a westerly wind (Fig. 6(e)) and remains like this until sunset. During the night (Fig. 6(f)), the wind speed decreases to a value close to that observed in the early morning, while the wind direction remains at westerly directions.

Before embarking on a detailed study of turbulent sea-spray transport, we need to select the proper numerical domain (d02, d01, d00) for analyzing the simulation results. For d02, the turbulence is entirely modeled by the subgrid model, while large-scale turbulence structures are explicitly re-

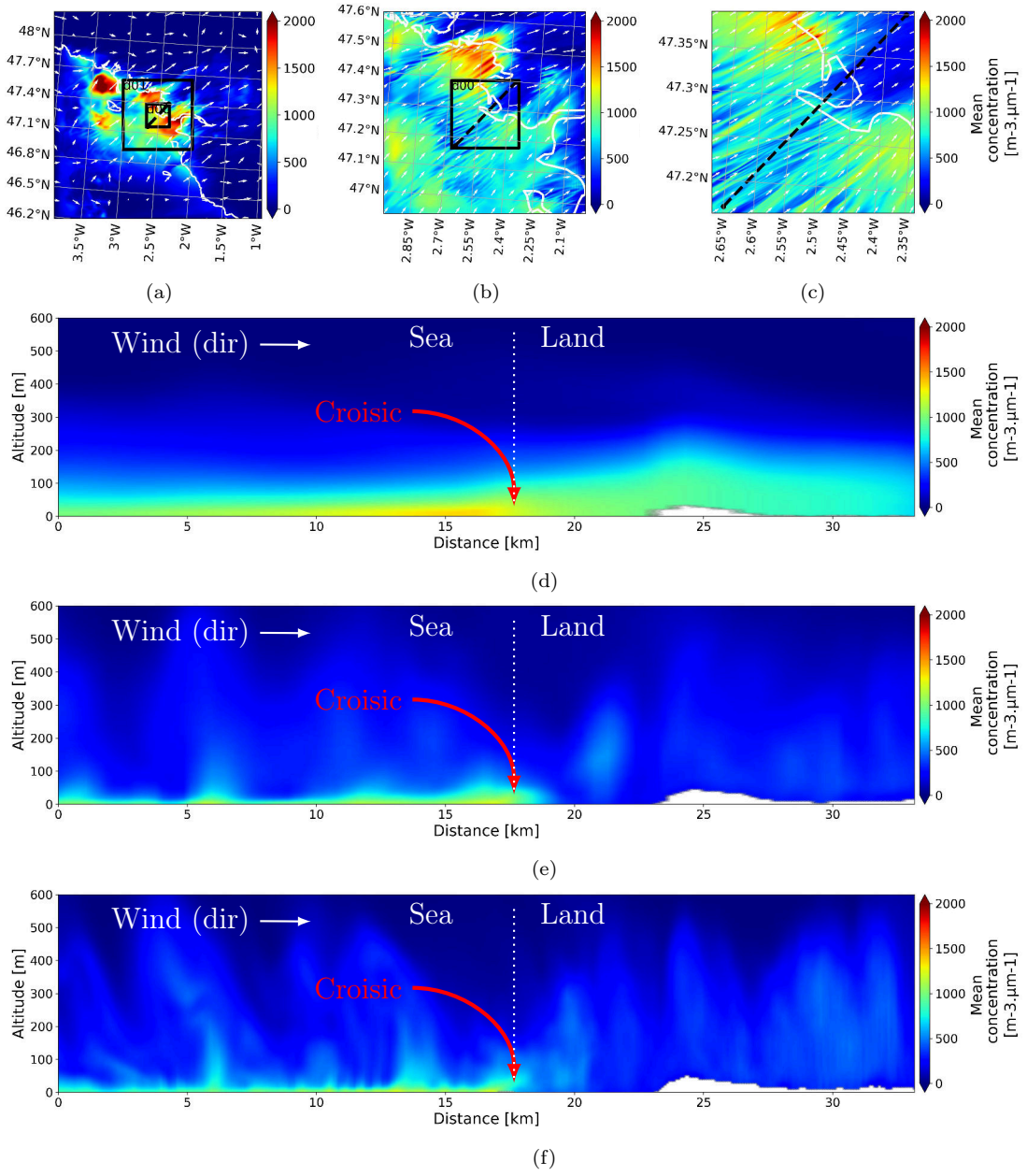

Figure 7: Averaged sea-spray concentration [$m^{-3}.\mu m^{-1}$] for $r_b = 5$ μm at 12:00 UTC on 18 June 2020 for domains: d02 (a, d), d01 (b, e) and d00 (c, f). Horizontal cross-sections at 20 m a.g.l. (a, b and c) and vertical cross-sections (d, e and f) indicated by the black dashed line in (a), (b) and (c), are presented. The white vectors indicate the wind velocity. The colours represent the sea-spray concentration. Topographic elements are in white in (d), (e) and (f).

solved in d01 and d00. As an example of the influence of wind field on the sea-spray concentration, we plot in Fig. 7 the averaged concentration for $r_b = 5$ μm in the three domains at 12:00 UTC. Figs. 7(a-c) show the horizontal cross-section of concentration at 20 m a.g.l. The concentration field is quite different between d02 on the one hand, and d01 and d00 on the other hand. In the low-resolution domain (d02), the concentration field is quite homogeneous over the sea, far from the coast. In contrast, the concentration field in the higher-resolution domains (d01 and d00) is organized in elongated structures that resemble the streaky structures of the wind field (see Fig. 6(c) for a direct comparison with Fig. 7(c)). We also note in d02 some high-concentration spots where the coast has an irregular shape or near the largest island (Belle-île). In particular, the high values of sea-spray concentration that are simulated in d02 over the Loire estuary (located around the coordinate 47.25°N and 2.5°W) are not observed in the higher-resolution domain d01.

Figs. 7(d-f) depict the vertical cross-sections of the domains along the black dashed line indicated in each of the top panels. An arrow indicates the location of Le Croisic. Note that several kilometers separate Le Croisic from the place where the land begins to rise notably above sea level. When comparing the three concentration fields, we note that the vertical transport of sea spray is much more efficient in the inner domains d01 and d00 than in the outer domain d02 where the aerosols remain relatively close to the surface. This was expected as the LES model solves smaller turbulent structures on the finer meshes (d01 and d00).

Another important difference appears between low- and high-resolution simulations: the sea-spray concentrations over land drop markedly when the airmass reaches the land in the domains d01 and d00, but not in d02. This suggests a significant influence of the coastal transition on dispersion processes, which is expected to be better simulated at high resolution. With the low resolution in d02, the model fails to reproduce the main characteristics of the aerosol transport. This can be explained by the so-called gray zone of turbulence (Wyngaard, 2004), where neither LES turbulence models nor Planetary Boundary Layer (PBL) parameterizations can correctly represent the turbulent process in the ABL. It could be argued that the d01 domain is at the limit of the gray zone of turbulence. Indeed the review of Honnert et al. (2020) suggests that the Convective Boundary Layer gray zone is in the range of 200-400 m of horizontal resolution, but that the behavior of the models in this gray zone also depends on the physical parameters of the

simulation and numerical characteristics of the model. Our simulations show a clear discrepancy in the concentration field simulated in d02 compared to the two other domains (d00 and d01), whereas the results obtained in d01 and d00 are comparable (with an expected smoothing due to the lower resolution in d01). We believe the sea-spray behavior observed in high-resolution domains (d01 and d00) to be more realistic and we are reasonably confident in using the results of the simulation d01 to study the turbulence effect on the sea-spray concentration in Sec. 4.2.

In order to highlight the difference between individual sea-spray bins, Fig. 8 shows, in a similar presentation as Fig. 7, the horizontal and vertical cross-sections of sea-spray concentrations for three different bins, i.e., $r_b \in \{2.5,\ 10.0,\ 20.0\}$ μm. All data shown originates from domain d00. The horizontal cross-sections (Figs. 8(a-c)) show similar organization of the concentration field for all three radii, consisting of elongated structures of higher concentration originating from the South-West. The results presented in Fig. 7(c) for $r_b = 5.0$ μm fit nicely in this series. Note that the concentration scale (false colour scale) differs between the plots. This demonstrates the difference in the strengh of aerosols production, which is higher for the smaller radii. We also note that the elongated structures are wider and cover longer distances when the radius is smaller. This shows the better efficiency of transport and diffusion processes of these smaller sea-spray particles. The vertical cross-sections (Figs. 8(d-f)) confirm this trend, with similar structures observed for all individual radii, but far less extended in altitude as the radius increases. In addition, sedimentation may play a role as larger particles are heavier and deposite faster on the surface. In Sec. 4.2, we will focus on aerosols of size $r_b = 5.0$ μm for which the production process dominates and the simulated concentration compares favorably to ANAM and the experimental observations (see Fig. 4).

The observation of the wind conditions indicate a day of almost directionaly constant wind with slowly evolving magnitude. Despite this seemingly uncomplicated weather, the spatial distribution of sea-spray concentration was found to be highly inhomogeneous. The wind variations associated to large-scale turbulent structures over the sea are apparently sufficient to create well-defined structures of low and high concentrations. These structures appear for all aerosol radii, although the concentration is higher for smaller aerosols for which production and transport are more efficient. The coastline

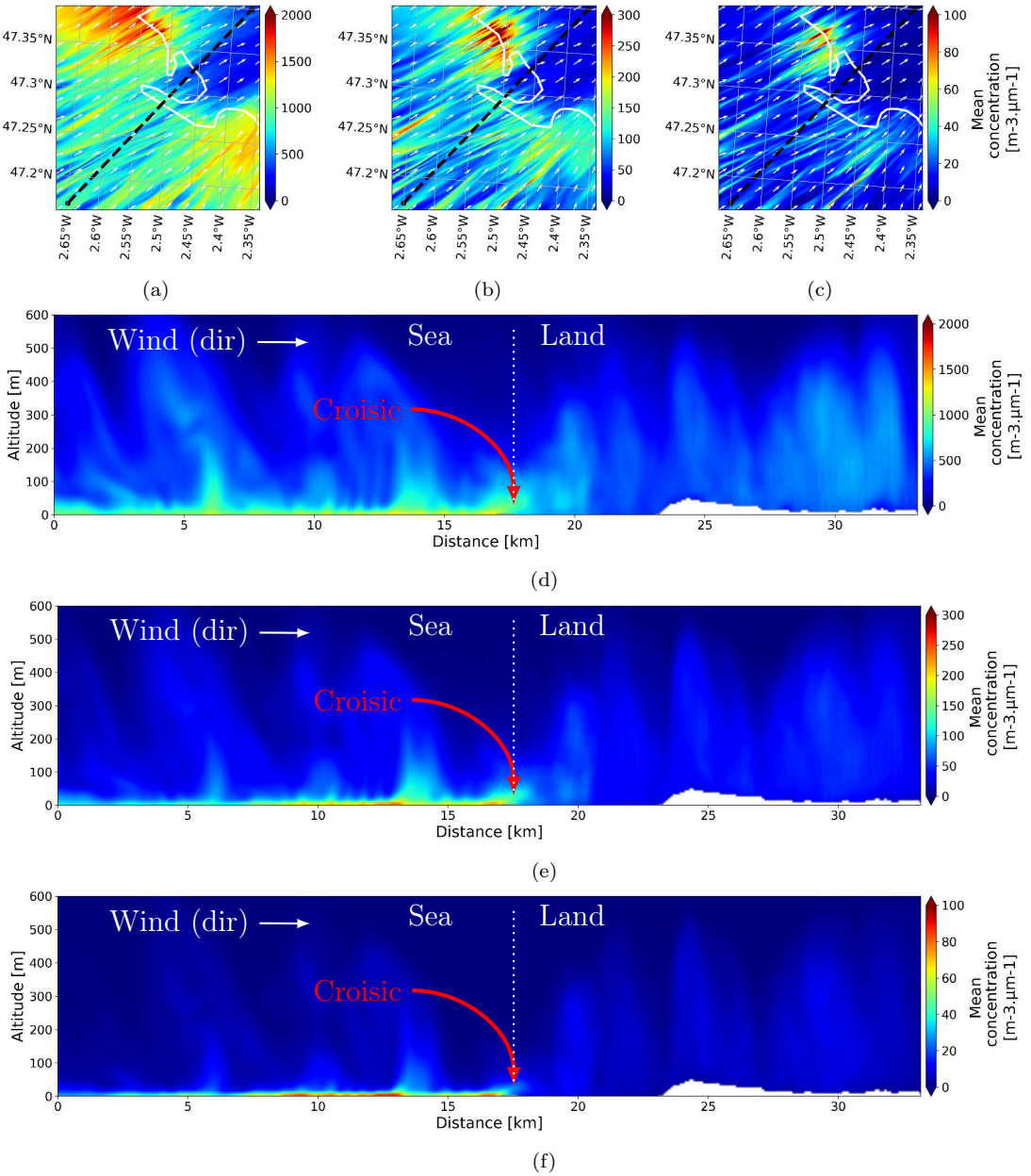

Figure 8: Averaged sea-spray concentration [$m^{-3}.\mu m^{-1}$] in domain d00 at 12:00 UTC on 18 June 2020 for different radii r_b: 2.5 μm (a and d), 10 μm (b and e) and 20 μm (c and f). Horizontal cross-sections at 20 m a.g.l. (a, b and c) and vertical cross-sections (d, e and f) indicated by the black dashed line in (a), (b) and (c), are presented. The white vectors indicate the wind velocity. The colours represent the sea-spray concentration. Topographic elements are in white in (d), (e) and (f).

appears as a clear transition in the behavior of particles produced over the sea.

4.2. Turbulence effect on the sea-spray concentration

We now investigate the different behavior, over the sea and over land, of sea-spray aerosols of size $r_b = 5.0$ μm, with particular attention to how the coastal area modifies the wind field and turbulence, and thereby the sea-spray transport in the ABL. We focus on the intermediate domain d01 which offers a good compromise between a detailled view of the processes at the local sea-land transitions and a general view over sea and land. The following analysis is based on events occuring on 18 June 2020 at 06:00 UTC, 14:00 UTC and 20:00 UTC, corresponding to periods just after sunrise, during the day and at sunset, respectively.

Fig. 9 presents the mean sea-spray concentration $\bar{c}_b$ for $r_b = 5.0$ μm in horizontal cross-sections at 20 m a.g.l. (Figs. 9(a-c)) and in vertical cross-sections (Figs. 9(d-f)) that are closely aligned with the wind direction and allow studying the aerosol transport across the sea-land interface. However, at 20:00 UTC the wind is not as well aligned with the vertical cross-section as at the two other times (see Figs. 9(a-c)), resulting most certainly in a transport from westerly directions, and thereby creating higher concentrations than if the transport was strictly along the transect.

These three snapshots illustrate the complex patterns of the aerosol concentrations over the full day. Striking differences in aerosol transport between daytime (14:00 UTC) and (close to) nighttime (06:00 and 20:00 UTC) are highlighted in Fig. 9. Note that the concentration (false color) scales again differ for individual plots. Whereas the sea spray penetrates fairly well inland at night, there seems to be a barrier during the day at the coast or further inland where the terrain starts to rise. This barrier appears despite stronger wind conditions which favour both the production of marine aerosols and their downwind transport. Near-surface concentrations remain low over land during the day (Fig. 9(e)) in comparison with the high concentration of aerosols in the 20 km zone off the coast and in contrast with the situation in the early morning (Fig. 9(d)) and evening (Fig. 9(f)) when the aerosols remain closer to the surface and propagate far inland.

These observations are explained by the efficiency of the vertical dispersion of the aerosols through the atmospheric boundary layer. The vertical dispersion of sea spray is initiated at 07:00 UTC (not shown here) by the appearance of plume-like structures over the sea, 20 to 40 km offshore. These

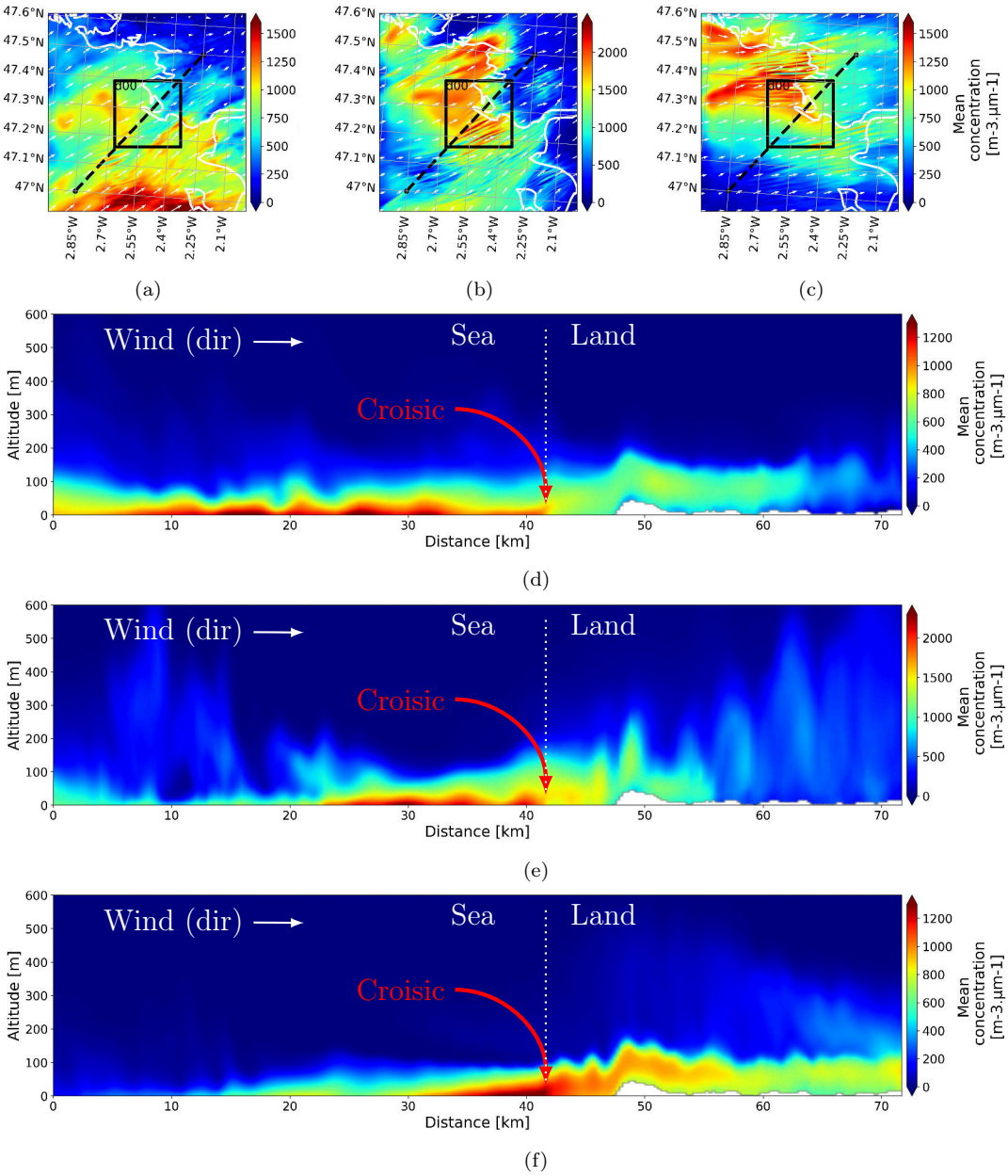

Figure 9: Averaged sea-spray concentration $\bar{c}_b$ [$\mathrm{m}^{-3}.\mu\mathrm{m}^{-1}$] for r_b = 5.0 μm in domain d01 at different times on 18 June 2020: 06:00 UTC (a and d), 14:00 UTC (b and e) and 20:00 UTC (c and f). Horizontal cross-sections at 20 m a.g.l. (a, b and c) and vertical cross-sections (d, e and f) indicated by the black dashed line in (a), (b) and (c), are presented. The white vectors indicate the wind velocity. The colours represent the sea-spray concentration. Topographic elements are in white in (d), (e) and (f).

structures intensify during the morning until 14:00 UTC (Fig. 9(e)). At that time, similar plumes have appeared over land, suggesting an efficient vertical dispersion of the aerosols transported onto the land. After sunset (Fig. 9(f)), the plumes have mostly disappeared, but their imprint remains present aloft, as a residual of the daytime mixing. Our simulations indicate that the 5.0 μm aerosols lifted upwards can reach heights of 600 m or more.

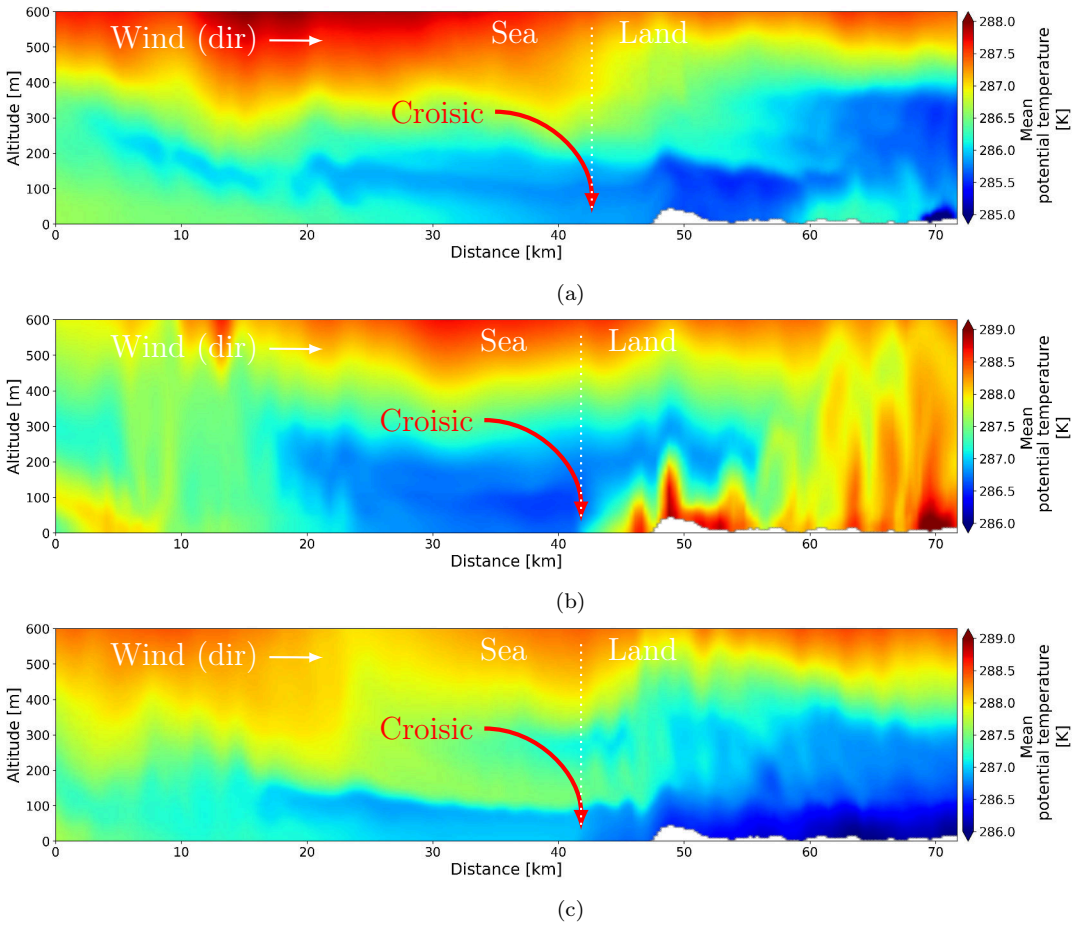

Figure 10: Averaged potential temperature $\bar{\theta}$ [K] on domain d01 at different times on 18 June 2020: 06:00 UTC (a), 14:00 UTC (b) and 20:00 UTC (c). The same vertical cross-sections as in Fig. 9 are presented.

This behavior can be linked to the thermal stratification of the ABL, which can be revealed by the vertical gradient of the potential temperature. To this end, Fig. 10 presents the mean potential temperature $\bar{\theta}$ for the same

vertical cross-sections and timestamps as in Fig. 9. Over the sea, the thermal stratification of the lower layers of the ABL alternates between neutral or weakly unstable in the early morning (Fig. 10(a)) and evening (Fig. 10(c)), and stable during the day with some unstable areas far offshore (Fig. 10(b)). Above the land, the atmosphere is stable after sunset (20:00 UTC, Fig. 10(c)) and at night (not shown). Just after sunrise (06:00 UTC, Fig. 10(a)) the thermal stratification becomes neutral and then evolves towards unstable conditions, as evidenced at 14:00 UTC by the vertical structures in the potential temperature field (Fig. 10(b)). The figure also shows the intrusion of cooler marine air over the first 15 km of the land surface. In this zone, the thermal structures are confined to about 150 m above the land surface and topped by the stable upwind marine atmosphere. The ABL structure over land is typical of the development of a thermal (convective) Internal Boundary Layer (IBL), which is replaced further inland by a well-mixed convective boundary layer (Calmet and Mestayer, 2016).

During the day (at 14:00 UTC) the comparison between potential temperature (Fig. 10(b)) and concentration fields (Fig. 9(e)) reveals the similarity between the vertical thermal structure of the ABL and the vertical concentration plumes. This is observed over land and also over the sea (between 5 and 15 km), i.e., in the regions where a convective boundary layer is present. This observation, combined with the values of concentrations quite well mixed in the whole ABL, suggests that sea-spray aerosols advected close to the ground (or produced at the sea surface) can be lifted by intense convective motions, then mixed throughout the full vertical extent of the atmospheric boundary layer.

In the presence of weak thermal effects, i.e., in a quasi-neutral atmosphere, turbulence generated by the wind shear and the friction at the surface may play a role in the aerosol dispersion. Along the transect, the surface roughness increases over several orders of magnitude, with marshland just behind the sea-land transition and rougher, drier surfaces beyond the topographic feature. As a result, the mechanical turbulence may change accordingly near the surface (Kaimal and Finnigan, 1994). To verify this, the resolved TKE computed with Eq. (12) is presented in Fig. 11. None of the timeframes presented here show the clear signature of the change in surface roughness that would favour the production of mechanical turbulence when moving from sea to land. This is explained by the influence, all day long, of heat transfers between the various surfaces and the atmosphere, and thereby, by the thermal stability of the atmosphere. Consequently, areas along the transect charac-

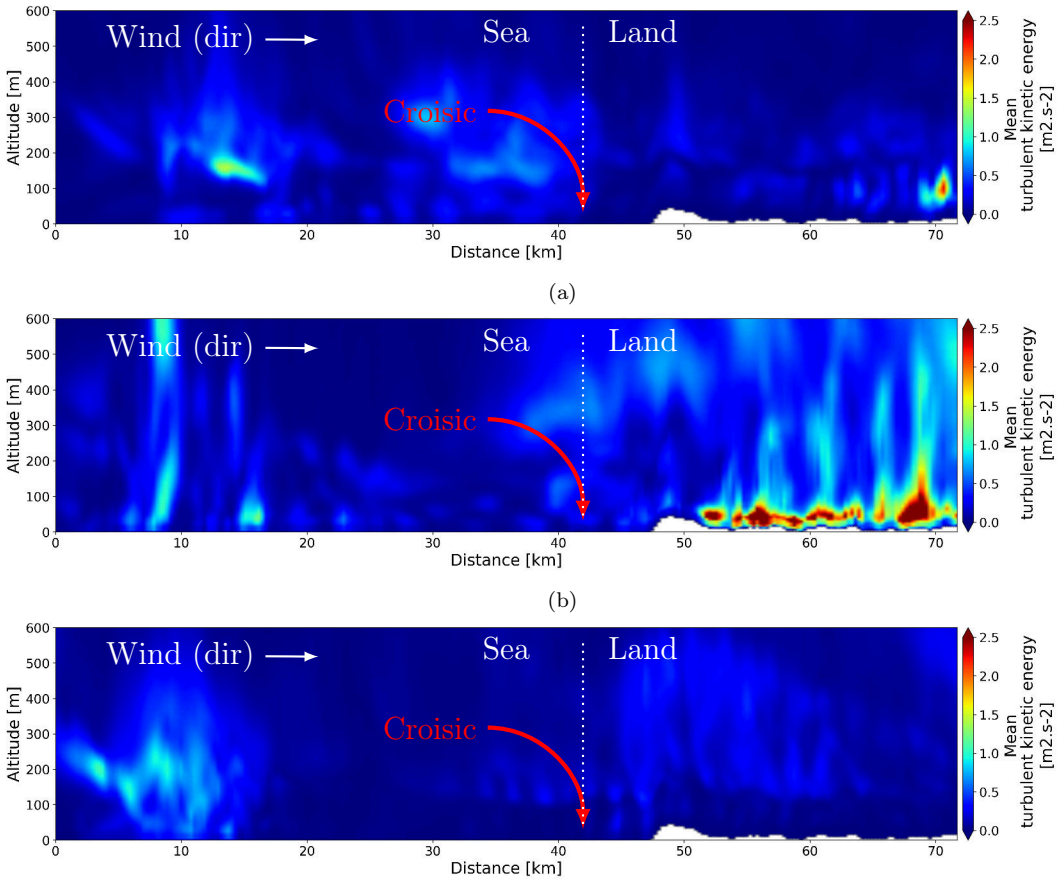

Figure 11: Turbulent Kinetic Energy $\overline{k}$ [$m^2.s^{-2}$] on domain d01 at different times on 18 June 2020: 06:00 UTC (a), 14:00 UTC (b) and 20:00 UTC (c). The same vertical cross-sections as in Fig. 9 are presented.

terized by neutral or stable stratification of the lower atmosphere experience low TKE values compared to the high values observed above the land under unstable atmospheric conditions. However, in the regions of quite low turbulence over the sea, as at 06:00 and 14:00 UTC, the succession of higher and lower values of TKE (Fig. 11(a-b)) roughly coincides with the oscillations in the thickness of the aerosol layer (Fig. 9(d-e)). This suggests that the initial dispersion processes near the surface is governed by local turbulence. Above the land area with strong thermal turbulence (14:00 UTC, Fig. 11(b)), initial vertical dispersion in the unstable atmospheric surface layer combines with

vertical transport by convective cells and turbulence aloft, giving rise to efficient aerosol mixing (Fig. 9(e)). Finally, in the early evening characterized by a stable layer over land, the presence of aerosols in the upper layer of the ABL (Fig. 9(f)) corresponds fairly well to the TKE field. This suggests that turbulence in the residual layer, even if not very intense, has an effect on aerosol dispersion.

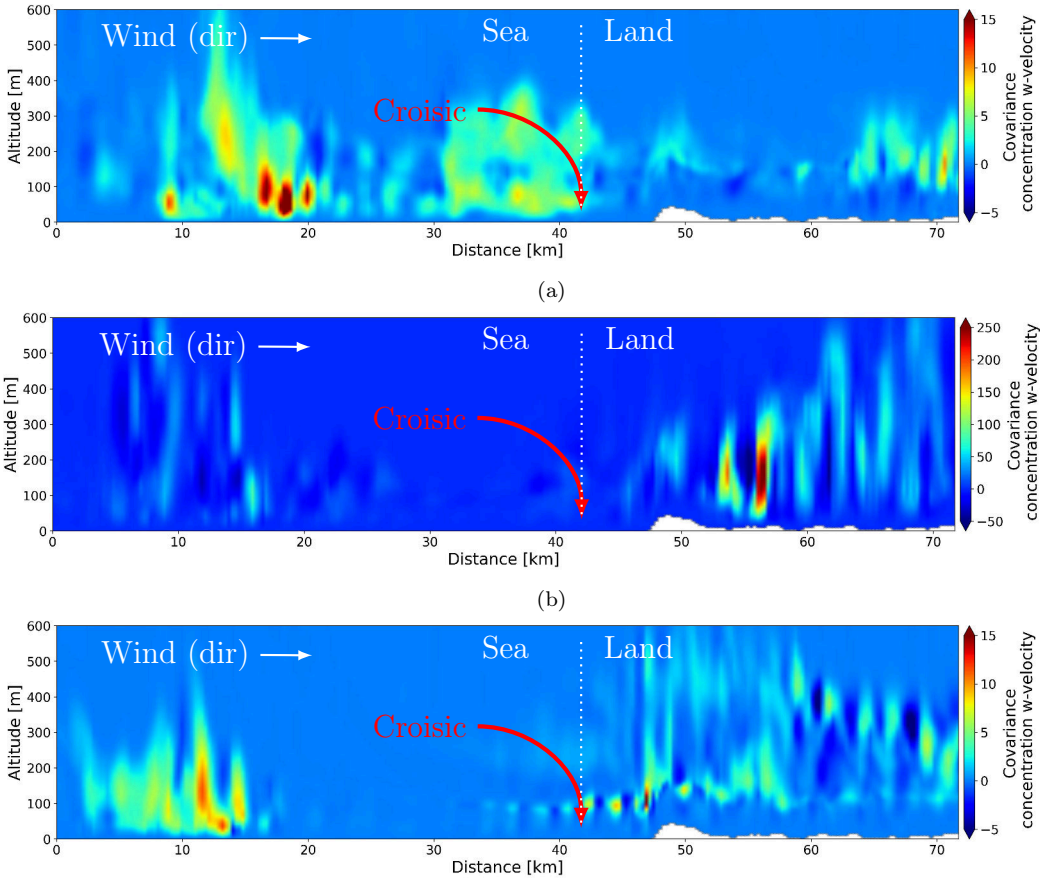

Figure 12: Vertical turbulent flux $\overline{c'w'}$ [$\mathrm{m}^{-2}.\mathrm{s}^{-1}.\mu\mathrm{m}^{-1}$] of sea-spray aerosols ($r_b = 5.0$ μm) on domain d01 at different times on 18 June 2020: 06:00 UTC (a), 14:00 UTC (b) and 20:00 UTC (c). The same vertical cross-sections as in Fig. 9 are presented.

To further investigate how turbulence affects the vertical mixing of sea-spray aerosols, the covariance $\overline{c'w'}$ between c_b and the vertical velocity w is

presented in Fig. 12. The figure evidences the signature of turbulence in the aerosol dispersion, and the intensity of the covariance is closely related to the vertical structure of the ABL and the vertical concentration gradients. Over the sea, the regions characterized by a moderately unstable atmosphere (in the morning, evening and in the middle of the day far from the coast) experience significant values of $\overline{c'w'}$. Depending on the vertical extent of the domain in which the flux acts, this turbulent processes can either drastically lower the aerosol concentration near the surface, or induce a succession of locally higher and lower concentrations near the surface and associated oscillations in the aerosols layer. Over the land, in the early morning (Fig. 12(a)) and evening (Fig. 12(c)), the neutral or weakly stable near-surface layers lead to an almost complete absence of turbulent vertical flux. This explains why the aerosols remain confined to the near-surface layer (see Fig. 9(d,f)). However, a turbulent concentration flux exists at the upper boundary of the aerosol layer, due to the strong gradient of concentration. Above this layer, the flux $\overline{c'w'}$ takes higher values and extends to higher altitude in the early evening: this is explained by the presence of turbulence in the residual layer that also contains aerosols because of the vertical mixing during daytime. Evidence for the latter process is provided by Fig. 12(b) which shows very high values of $\overline{c'w'}$ above land after the flow passes the small hill at roughly 50km distance into the domain, in accordance with the strong TKE (Fig. 11(b)). This reinforces the convective transport that is initiated by the unstable stratification (see Fig. 10(b)), resulting in aerosols being dispersed aloft (see Fig. 9(e)).

The turbulence-induced vertical flux of sea-spray aerosols at the sea-land transition has previously been studied by Liang and Yu (2016) for an academic scenario with flat surfaces, homogeneous surface heat flux and homogeneous sea-spray production. Although our configuration is more complex, their results generally corroborate ours, i.e., $\overline{c'w'}$ is very weak under neutral atmospheric stability (and even weaker under stable stratification) and increases with increasing surface heat flux. For their analysis, Liang and Yu (2016) defined z_{c_m} and z_{w_m} as the altitudes at which $\overline{c'w'}$ and the vertical velocity fluctuations σ_w attain their maxima, respectively, and R_{cw} as the ratio between z_{c_m} and z_{w_m}. Although not explicitly mentioned in their paper, their analysis certainly refers to the production term in the $\overline{c'w'}$ budget equation, which reduces to $-\sigma_w^2 \dfrac{\partial \overline{c}_b}{\partial z}$ for a horizontally homogeneous flow. Focusing on the turbulent transport of aerosols in the convective Internal Boundary Layer, Liang and Yu (2016) found that $R_{cw} > 1$ in the first stages of IBL

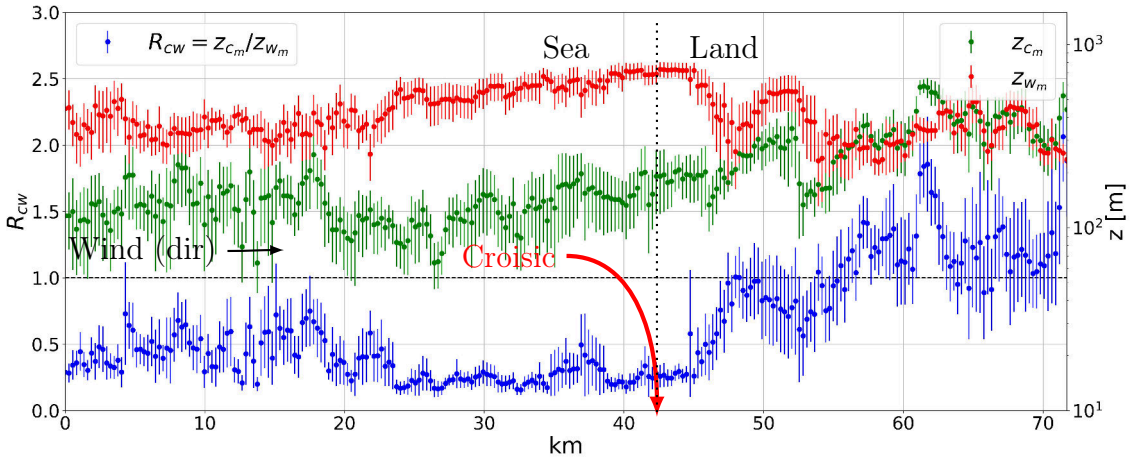

Figure 13: Variation of $R_{cw} = \frac{z_{c_m}}{z_{w_m}}$ (left axis) and corresponding z_{c_m} and z_{w_m} (Right axis in log scale) along the transect (see Fig. 9). Dots represent the mean of 15-minutes data points calculated between 13:00 and 15:00 UTC, vertical bars represent standard deviations.

development and $R_{cw} \approx 1$ when the IBL was fully developed. Excluding other possible contributions to $\overline{c'w'}$ related to the inhomogeneity at the sea-land transition, Liang and Yu (2016) attributed the difference between z_{c_m} and z_{w_m} to the large vertical concentration gradient in the upper part of the developing IBL.

Of the three periods presented here, 14:00 UTC is the one that most closely resembles the situation studied by Liang and Yu (2016). For comparison purposes, Fig. 13 shows the values of z_{c_m}, z_{w_m} and R_{cw}, determined at each horizontal grid position along the transect by averaging the 15-minutes statistics over a 2-hour timeframe (13:00-15:00 UTC). In this period (around 14:00 UTC), the thermal stability of the atmosphere was identified as varying along the transect (Fig. 10(b)): over the sea, it is weakly unstable (from 0 to around 20 km) and neutral to stable (from around 20 to 40 km); over land, it is unstable in the lower layers, with convective structures developing in height as the fetch increases. In the first part of the transect, the values of R_{cw} oscillate around 0.5, indicating that the height, at which the maximum of $\overline{c'w'}$ is reached, is lower than the height at which vertical velocity fluctuations are at their maximum. This is even more so for the second part of the transect, where R_{cw} attains values around 0.25. The significant difference between z_{c_m} and z_{w_m} in the neutral and stable marine ABL reflects

the inefficient vertical turbulent transport of aerosols. As demonstrated by Fig. 9(e), the aerosol concentration gradient is generally greater just above the sea-spray production area, explaining why over sea the z_{c_m} is always smaller than z_{w_m} regardless of the stability.

In the third part of the transect where a thermal IBL could develop over the land, the aerosols are first trapped in a relatively thin layer (Fig. 9(e)), resulting in values of R_{cw} as low as over the sea. As the flow penetrates further inland, the vertical gradient of concentration is progressivly smoothed and R_{cw} rapidly increases to a value of 1 (as observed by Liang and Yu (2016) for the fully developed thermal IBL), reflecting the increasing efficiency of turbulent mixing. However, the disturbance induced by the main topographic feature (around 50 km) seems to interrupt the theoretical development of the IBL, causing R_{cw} to decrease (km 50-53), then increase (km 53-59) before starting to oscillate between values greater than 1, which could be the sign of the well-mixed layer. In conclusion, after the sea-land transition, the turbulence plays an important role in explaining the aerosol vertical transport, but in a complex interaction with other processes such as the vertical transport by convective cells and flow modifications induced by topography.

5. Conclusion

This paper presents a numerical study of sea-spray generation and transport by mean wind and turbulence in the coastal area of Le Croisic (Brittany, France). To this end, a set of nested simulations have been carried out for a summer day (18 June 2020) during which the southwesterly wind is conducive to studying the behavior of aerosols at the sea-land transition and their transport over land. The two largest domains have been simulated by WRF with ERA5 meteorological forcing, providing the mesoscale atmospheric conditions along the day. Aerosol dynamics were then simulated in three higher-resolved, nested domains, using the ARPS Large-Eddy Simulation model in which marine aerosol models had been implemented. The Bruch et al. (2021) source function was used to generate the sea-spray aerosols, which were subsequently transported through the computational domains.

The LES results have been checked against wind-LiDAR observations and data from ground-based meteorological stations, and were found to satisfac-

torily reproduce the measured wind field from the early morning to nighttime. Subsequently, the simulated concentrations of sea-spray aerosols were favorably compared to the parametric ANAM model and experimental data obtained with optical particle counters. Vertical profiles of the aerosol concentrations were found to be exponential, in accordance with Toba (1965)'s law. A qualitative analysis of the behavior of aerosols of different sizes confirmed the reliability of the ARPS model, particularly for the higher-resolution simulations where turbulent structures are better resolved.

For the study of turbulent transport of sea-spray in the coastal area, we focussed on aerosols of radius $r_b = 5.0$ μm and considered timeframes representative of typical thermal stability over the sea and over land : around sunrise, in the afternoon and after sunset. The aerosol behavior was analyzed in terms of the thermal stratification of the ABL over the sea and over land, and the dynamic and thermodynamic flow modifications that occur at the sea-land transition and further inland. Over the sea where aerosols are produced, a quasi-neutral thermal stability in the atmospheric surface layer results in variations of TKE intensity associated with high- and low-momentum structures, which govern both the production of aerosols and local dispersion by turbulence, as identified by oscillations in the thickness of the aerosol layer. A change in thermal stratification from neutral to stable leads to more homogeneous production of sea-spray aerosols and very weak vertical dispersion. Regardless of the thermal stratification in the marine atmospheric surface layer, the turbulent vertical flux of aerosol is explained by the vertical gradient of concentration, which always reaches a maximum at a lower altitude than the maximum vertical velocity, leading to relatively low vertical dispersion by turbulence. As a consequence, the aerosols are efficiently transported away from their production zone towards the sea-land interface and subsequently inland.

At nighttime, when the atmosphere above land is stable, sea-spray aerosols are confined in the first hundred meters above the surface. In contrast, the daytime unstable stratification over land induces increasingly efficient vertical turbulent dispersion of aerosols, as the thermal IBL develops with fetch and transforms further inland into a well-mixed boundary layer. Here, the unstable stratification gives rise to intense thermal turbulence (as evidenced by significant values of TKE near the surface), which in turn creates convective cells. The large-scale convective motions combine with turbulent vertical transport of aerosols and are likely the main cause for the observed aerosol

concentration plumes.

Although focused on a specific coastal area, this study based on a LES approach demonstrates that sea-spray aerosol dispersion in coastal areas is a complex process that requires considering both small-scale turbulence and larger-scale ABL structures, both of which vary as a function of the thermal stability of the atmosphere along the diurnal cycle and small-scale topographical features. To explore this further, it would be interesting to consider the influence of sea-spray aerosols on the land surface radiative budget that governs the cooling and warming of the surface. However, this step would certainly require a more accurate modeling of the aerosol production (especially in the surf zone) and their transformations.

Acknowledgements

This research has been supported by ANR-ASTRID under the contract ANR-18-ASTR-0002 and by the France Atlantique project founded by the French "Agence de l'Environnement et de la Maîtrise de l'Energie", through the France 2030 program. Numerical simulations were performed by using HPC resources from Centrale Nantes Supercomputing Centre ICI-CNSC on the cluster Liger. Finally, we would like to thank the SEM-REV team who helped with the on-site measurement. A CC-BY public copyright license has been applied by the authors to the present document and will be applied to all subsequent versions up to the Author Accepted Manuscript arising from this submission, in accordance with the grant's open access conditions.

Appendix A. ARPS, soil types and vegetation types

To simulate real conditions, we need a correct land description both in soil and vegetation coverage. For the former, Tab. A.1 presents the 13 soil classes used by ARPS. A two-step procedure is used to attribute a specific soil class to a surface mesh. First, we consult a specific ESDAC database that gives the percentage of sand, silt and clay in the soil. The official USDA soil texture triangle is subsequently used to identify the appropriate soil class, which corresponds on an almost one-to-one basis with the soil types available in ARPS. The ESDAC database does not contain entries for ice, water or urban surfaces. In these cases, the CLC 2018 database provides the soil type. Since the CLC database contains a large number of surface types, a mapping had to be performed. As an example, Tab. A.1 shows that all CLC urban

surface types (index 1 through 9) have been mapped on soil type 3 of ARPS (Clay Loam).

The vegetation coverage was exclusively retrieved from the CLC 2018 database, and again a mapping scheme was necessary as depicted in Tab.A.2. Each CLC vegetation type is associated with a roughness length z_0. The Table shows that these values do not always correspond well with the value provided for the ARPS vegetation type that the CLC types are mapped onto. Nevertheless, we used the ARPS value as-is, without attempting to take into account the CLC suggestions. On the other hand, when a specific mesh contained multiple ARPS vegetation types, an average of the ARPS roughness lengths was taken.

The Leaf Area Index (LAI), used for thermodynamic balance between the vegetation and atmospheric temperature and humidity, is computed from the Normalized Difference Vegetation Index (NDVI) according to the ARPS vegetation type. The NDVI is obtained from the WEKEO (Copernicus) database. According to the vegetation type ID (v_i) given in the table A.2, the ARPS model is:

$$LAI = \begin{cases} 0.0 & \text{if } v_i \in \{9, 14\} \\ -\ln\left(\left[1 - \dfrac{NDVI}{0.915}\right]/0.83\right)/0.96 & \text{if } v_i \in \{1, 2, 3, 4, 5, 10, 11, 12, 13\} \\ 1.623 \times \exp\left(NDVI/0.34\right) & \text{if } v_i \in \{7, 8, 9\} \end{cases} \tag{A.1}$$

Table A.1: ARPS default soil type with corresponding Corine Land Cover 2018 corrections.

ARPS ID	SOIL TYPE	CLC ID	CLC TYPE
1	Sand	30 (331)	Beaches, dunes, sands
2	Loamy sand	N/A	N/A
3	Sandy loam	N/A	N/A
4	Silt loam	N/A	N/A
5	Loam	N/A	N/A
6	Sandy clay loam	N/A	N/A
7	Silty clay loam	N/A	N/A
3	Clay loam	1 (111)	Continuous urban fabric
		2 (112)	Discontinuous urban fabric
		3 (121)	Industrial or commercial units
		4 (122)	Roads and rail networks and associated land
		5 (123)	Port areas
		6 (124)	Airports
		7 (131)	Mineral extraction sites
		8 (132)	Dump sites
		9 (133)	Construction sites
9	Sandy clay	N/A	N/A
10	Silty clay	N/A	N/A
11	Clay	39 (423)	Intertidal flats
12	Ice	34 (335)	Glaciers and perpetual snows
13	Water	35 (411)	Inland marshes
		37 (421)	Salt marshes
		38 (422)	Salines
		40 (511)	Water courses
		41 (512)	Water bodies
		42 (521)	Coastal lagoons
		43 (522)	Estuaries
		44 (523)	Sea and oceans

Table A.2: ARPS default vegetation type and default roughness length z_0 with corresponding Corine Land Cover 2018 and choosen roughness length.

ARPS ID (v_i)	ARPS VEGETATION TYPE	z_0 (ARPS)	CLC ID	CLC TYPE	z_0
1	Desert	0.011	1 (111)	Continuous urban fabric	1.8
			2 (112)	Discontinuous urban fabric	0.5
			3 (121)	Industrial or commercial units	0.5
			4 (122)	Roads and rail networks and associated land	0.075
			5 (123)	Port areas	0.5
			6 (124)	Airports	0.01
			7 (131)	Mineral extraction sites	0.01
			8 (132)	Dump sites	0.01
			9 (133)	Construction sites	0.5
			30 (331)	Beaches, dunes, sands	0.003
			31 (332)	Bare rocks	0.01
2	Tundra	0.076	32 (333)	Sparsely vegetated areas	0.01
3	Grassland	0.075	26 (321)	Natural grasslands	0.03
4	Grassland with shrub cover	0.238	27 (322)	Moors and heathland	0.03
			28 (323)	Scelerophyllous vegetation	0.03
5	Grassland with tree cover	0.563	10 (141)	Green urban areas	0.6
			22 (244)	Agro-forestry areas	0.3
			29 (324)	Transitional woodland-shrub	0.6
6	Deciduous forest	0.826	24 (312)	Coniferous forest	1.3
			25 (313)	Mixed forest	1.3
7	Evergreen forest	1.089	23 (311)	Broad-leaved forest	1.3
8	Rain forest	2.653	N/A	N/A	N/A
9	Ice	0.011	34 (335)	Glaciers and perpetual snows	0.006
10	Cultivation	0.075	12 (211)	Non-irrgated arable land	0.05
			13 (212)	Permanently irrigated land	0.05
			14 (213)	Rice fields	0.05
			15 (221)	Vineyard	0.1
			16 (222)	Fruit trees and berry plantations	0.1
			17 (223)	Olive groves	0.1
			18 (231)	Pastures	0.03
			19 (241)	Annual crops associated with permanent crops	0.1
			20 (242)	Complex cultivation patterns	0.3
			21 (243)	Land principally occupied by agriculture, with significant areas of natural vegetation	0.3
11	Bog or marsh	0.1	35 (411)	Inland marshes	0.05
			36 (412)	Peat bogs	0.005
			37 (421)	Salt marshes	0.05
			38 (422)	Salines	0.005
			39 (423)	Intertidal flats	0.005
12	Dwarf shrub	0.856	11 (142)	Sport and leisure facilities	0.5
13	Semi-desert	0.065	33 (334)	Burnt areas	0.6
14	Water	0.002	40 (511)	Water courses	0.002
			41 (512)	Water bodies	0.002
			42 (521)	Coastal lagoons	0.002
			43 (522)	Estuaries	0.002
			44 (523)	Sea and oceans	0.002

References

Andreas, E.L., 1998. A new sea spray generation function for wind speeds up to 32 m/s. Journal of Physical Oceanography , 2175–2184URL: https://journals.ametsoc.org/view/journals/phoc/28/11/1520-0485_1998_028_2175_anssgf_2.0.co_2.xml.

Bauer, H.S., Muppa, S.K., Wulfmeyer, V., Behrendt, A., Warrach-Sagi, K., Späth, F., 2020. Multi-nested WRF simulations for studying planetary boundary layer processes on the turbulence-permitting scale in a realistic mesoscale environment. Tellus A: Dynamic Meteorology and Oceanography 72. URL: https://a.tellusjournals.se/articles/10.1080/16000870.2020.1761740.

Bruch, W., Piazzola, J., Branger, H., van Eijk, A.M.J., Luneau, C., Bourras, D., Tedeschi, G., 2021. Sea-spray-generation dependence on wind and wave combinations: A laboratory study. Boundary Layer Meteorology 180, 477–505. URL: https://doi.org/10.1007/s10546-021-00636-y.

Bruch, W., Yohia, C., Tulet, P., Limoges, A., Sutherland, P., van Eijk, A.M.J., Missamou, T., Piazzola, J., 2023. Atmospheric sea spray modeling in the north-east atlantic ocean using tunnel-derived generation functions and the sumos cruise dataset. Journal of Geophysical Research: Atmospheres 128, e2022JD038330. URL: https://doi.org/10.1029/2022JD038330.

Calmet, I., Mestayer, P., 2016. Study of the thermal internal boundary layer during sea-breeze events in the complex coastal area of marseille. Theoretical and Applied Climatology 123, 801–826. URL: https://doi.org/10.1007/s00704-015-1394-1.

Calmet, I., Mestayer, P.G., van Eijk, A.M.J., Herledant, O., 2018. A coastal bay summer breeze study, part 2: High-resolution numerical simulation of sea-breeze local influences. Boundary-Layer Meteorology 167, 27–51. URL: https://doi.org/10.1007/s10546-017-0319-1.

Chen, F., Dudhia, J., 2001. Coupling an advanced land surface–hydrology model with the penn state–ncar mm5 modeling system. part i: Model implementation and sensitivity. Monthly Weather Review 129, 569–585. URL: https://journals.ametsoc.org/view/journals/mwre/129/4/1520-0493_2001_129_0569_caalsh_2.0.co_2.xml.

Conan, B., Visich, A., 2024. Measurement and analysis of high altitude wind profiles over the sea in a coastal zone using a scanning wind lidar – application to wind energy. https://hal.science/hal-04734469 URL: https://hal.science/hal-04734469.

Cox, C., Munk, W., 1956. Slopes of the sea surface deduced from photographs of sun glitter. Scripps Inst. Ocean. .

Deardorff, J.W., 1980. Stratocumulus-capped mixed layers derived from a three-dimensional model. Boundary-Layer Meteorology 18, 495–527. URL: https://doi.org/10.1007/BF00119502.

Edson, J.B., Fairall, C.W., 1994. Spray droplet modeling: 1. lagrangian model simulation of the turbulent transport of evaporating droplets. Journal of Geophysical Research: Oceans 99, 25295–25311. URL: https://doi.org/10.1029/94JC01883.

van Eijk, A.M.J., Kusmierczyk-Michulec, J.T., Piazzola, J.J., 2011. The advanced navy aerosol model (anam): validation of small-particle modes, in: van Eijk, A.M.J., Hammel, S.M. (Eds.), Atmospheric Optics IV: Turbulence and Propagation, International Society for Optics and Photonics. p. 816108. URL: https://doi.org/10.1117/12.896178.

Fairall, C.W., D., K.J., G., H., 1995. The effect of sea spray on surface energy transports over the ocean. Global Atmopshere and Ocean Sysem 2, 121–142.

February, F.J., Piazzola, J., Altieri, K.E., Van Eijk, A.M., 2021. Contribution of sea spray to aerosol size distributions measured in a south african coastal zone. Atmospheric Research 262, 105790. URL: https://doi.org/10.1016/j.atmosres.2021.105790.

Ferrari, F., Rizza, U., Morichetti, M., Cassola, F., Miglietta, M.M., Mazzino, A., 2024. The role of atmospheric aerosols on severe convective precipitation in a mediterranean coastal region. Atmospheric Research 305, 107421. URL: https://doi.org/10.1016/j.atmosres.2024.107421.

Franco, I., Gutierrez, A., Cataldo, J., 2019. Effects of the surface and atmospheric stability on the integral length scale at a coastal site. Boudary-Layer Meteorology 172, 317–332. URL: https://doi.org/10.1007/s10546-019-00442-7.

Grythe, H., Ström, J., Krejci, R., Quinn, P., Stohl, A., 2014. A review of sea-spray aerosol source functions using a large global set of sea salt aerosol concentration measurements. Atmospheric Chemistry and Physics 14, 1277–1297. URL: https://doi.org/10.5194/acp-14-1277-2014.

Hersbach, H., Bell, B., Berrisford, P., Hirahara, S., Horányi, A., Muñoz-Sabater, J., Nicolas, J., Peubey, C., Radu, R., Schepers, D., Simmons, A., Soci, C., Abdalla, S., Abellan, X., Balsamo, G., Bechtold, P., Biavati, G., Bidlot, J., Bonavita, M., De Chiara, G., Dahlgren, P., Dee, D., Diamantakis, M., Dragani, R., Flemming, J., Forbes, R., Fuentes, M., Geer, A., Haimberger, L., Healy, S., Hogan, R.J., Hólm, E., Janisková, M., Keeley, S., Laloyaux, P., Lopez, P., Lupu, C., Radnoti, G., de Rosnay, P., Rozum, I., Vamborg, F., Villaume, S., Thépaut, J.N., 2020. The ERA5 global reanalysis. Quarterly Journal of the Royal Meteorological Society 146, 1999–2049. URL: https://onlinelibrary.wiley.com/doi/abs/10.1002/qj.3803, doi:10.1002/qj.3803.

Hiederer, R., 2013. Mapping soil properties for Europe : spatial representation of soil database attributes. Publications Office. URL: https://data.europa.eu/doi/10.2788/94128.

Honnert, R., Efstathiou, G.A., Beare, R.J., Ito, J., Lock, A., Neggers, R., Plant, R.S., Shin, H.H., Tomassini, L., Zhou, B., 2020. The atmospheric boundary layer and the "gray zone" of turbulence: A critical review. Journal of Geophysical Research: Atmospheres 125, e2019JD030317. URL: https://doi.org/10.1029/2019JD030317.

Jaenicke, R., 1982. Physical aspects of the atmospheric aerosol, in: Chemistry of the unpolluted and polluted troposphere, Springer. pp. 341–373. URL: https://doi.org/10.1007/978-94-009-7918-5_14.

Janssen, P.A.E.M., 1991. Quasi-linear theory of wind-wave generation applied to wave forecasting. Journal of Physical Oceanography 21, 1631–1642. URL: https://doi.org/10.1175/1520-0485(1991)021<1631:QLTOWW>2.0.CO;2.

Johansson, J.H., Salter, M.E., Navarro, J.A., Leck, C., Nilsson, E.D., Cousins, I.T., 2019. Global transport of perfluoroalkyl acids via sea spray aerosol. Environmental Science: Processes & Impacts 21, 635–649. URL: https://doi.org/10.1039/C8EM00525G.

Kaimal, J.C., Finnigan, J.J., 1994. Atmospheric Boundary Layer Flows: Their Structure and Measurement. Oxford University Press. URL: https://doi.org/10.1093/oso/9780195062397.001.0001.

Kepert, J., Fairall, C., Bao, J.W., 1999. Modelling the Interaction Between the Atmospheric Boundary Layer and Evaporating Sea Spray Droplets. Springer Netherlands. pp. 363–409. URL: https://doi.org/10.1007/978-94-015-9291-8_14.

Kim, G., Lee, J., Lee, M.I., Kim, D., 2021. Impacts of urbanization on atmospheric circulation and aerosol transport in a coastal environment simulated by the wrf-chem coupled with urban canopy model. Atmospheric Environment 249, 118–253. URL: https://doi.org/10.1016/j.atmosenv.2021.118253.

de Leeuw, G., 1989. Modeling of extinction and backscatter profiles in the marine mixed layer. Applied Optics 28, 1356–1359. URL: https://doi.org/10.1364/AO.28.001356.

de Leeuw, G., Andreas, E.L., Anguelova, M.D., Fairall, C.W., Lewis, E.R., O'Dowd, C., Schulz, M., Schwartz, S.E., 2011. Production flux of sea spray aerosol. Reviews of Geophysics 49. URL: https://doi.org/10.1029/2010RG000349.

Lenain, L., Melville, W.K., 2017. Evidence of sea-state dependence of aerosol concentration in the marine atmospheric boundary layer. Journal of Physical Oceanography 47, 69–84. URL: https://doi.org/10.1175/JPO-D-16-0058.1.

Lewis, E, R., Schwartz, S, R., 2004. Sea Salt Aerosol Production: Mechanisms, Measurements and Models - A Critical Review. American Geophysical Union. URL: https://www.doi.org/10.1029/GM152.

Liang, T., Yu, X., 2016. A numerical study of sea-spray aerosol motion in a coastal thermal internal boundary layer. Boundary-Layer Meteorology 160, 347–361. URL: https://doi.org/10.1007/s10546-016-0142-0.

Luo, H., Jiang, B., Li, F., Lin, W., 2019. Simulation of the effects of sea-salt aerosols on the structure and precipitation of a developed tropical cyclone. Atmospheric Research 217, 120–127. URL: https://doi.org/10.1016/j.atmosres.2018.10.018.

Mallet, M., Roger, J., Despiau, S., Dubovik, O., Putaud, J., 2003. Microphysical and optical properties of aerosol particles in urban zone during escompte. Atmospheric Research 69, 73–97. URL: https://doi.org/10.1016/j.atmosres.2003.07.001.

Mestayer, P.G., Van Eijk, A.M.J., De Leeuw, G., Tranchant, B., 1996. Numerical simulation of the dynamics of sea spray over the waves. Journal of Geophysical Research: Oceans 101, 20771–20797. URL: https://doi.org/10.1029/96JC01425.

Michioka, T., Chow, F.K., 2008. High-resolution large-eddy simulations of scalar transport in atmospheric boundary layer flow over complex terrain. Journal of Applied Meteorology and Climatology 47, 3150–3169. URL: https://doi.org/10.1175/2008JAMC1941.1.

Moeng, C.H., 1984. A Large-Eddy-Simulation Model for the Study of Planetary Boundary-Layer Turbulence. Journal of the Atmospheric Sciences 41, 2052–2062. URL: https://journals.ametsoc.org/view/journals/atsc/41/13/1520-0469_1984_041_2052_alesmf_2_0_co_2.xml, doi:10.1175/1520-0469(1984)041<2052:ALESMF>2.0.CO;2.

Mulcahy, J.P., O'Dowd, C.D., Jennings, S.G., Ceburnis, D., 2008. Significant enhancement of aerosol optical depth in marine air under high wind conditions. Geophysical Research Letters 35. URL: https://doi.org/10.1029/2008GL034303.

Niu, G.Y., Yang, Z.L., Mitchell, K.E., Chen, F., Ek, M.B., Barlage, M., Kumar, A., Manning, K., Niyogi, D., Rosero, E., Tewari, M., Xia, Y., 2011. The community Noah land surface model with multiparameterization options (Noah-MP): 1. Model description and evaluation with local-scale measurements. Journal of Geophysical Research: Atmospheres 116. URL: https://onlinelibrary.wiley.com/doi/abs/10.1029/2010JD015139, doi:10.1029/2010JD015139.

Peng, T., Richter, D., 2017. Influence of evaporating droplets in the turbulent marine atmospheric boundary layer. Boundary-Layer Meteorology 165, 497–518. URL: https://doi.org/10.1007/s10546-017-0285-7.

Piazzola, J., Mihalopoulos, N., Canepa, E., Tedeschi, G., Prati, P., Zarmpas, P., Bastianini, M., Missamou, T., Cavaleri, L., 2016. Characterization

of aerosols above the northern adriatic sea: Case studies of offshore and onshore wind conditions. Atmospheric Environment 132, 153–162. URL: https://doi.org/10.1016/j.atmosenv.2016.02.044.

Piazzola, J., Tedeschi, G., Demoisson, A., 2015. A model for the transport of sea-spray aerosols in the coastal zone. Boundary-Layer Meteorology 155, 329–350. URL: https://doi.org/10.1007/s10546-014-9994-3.

Pope, S, B., 2000. Turbulent Flows. Cambridge University Press.

Prandtl, L., 1952. Essential of Fluid Dynamics with Applications to Hydraulics, Aeronautics, Meteorology, and Other Subjects. Hafner Publishing Compagny.

QGIS Development Team, 2022. QGIS Geographic Information System. QGIS Association. URL: https://www.qgis.org.

Reid, J.S., Brooks, B., Crahan, K.K., Hegg, D.A., Eck, T.F., O'Neill, N., de Leeuw, G., Reid, E.A., Anderson, K.D., 2006. Reconciliation of coarse mode sea-salt aerosol particle size measurements and parameterizations at a subtropical ocean receptor site. Journal of Geophysical Research: Atmospheres 111. doi:10.1029/2005JD006200.

Richter, D., Chamecki, M., 2018. Inertial effects on the vertical transport of suspended particles in a turbulent boundary layer. Boundary-Layer Meteorology 167, 235–256. URL: https://doi.org/10.1007/s10546-017-0325-3.

Rizza, U., Canepa, E., Miglietta, M.M., Passerini, G., Morichetti, M., Mancinelli, E., Virgili, S., Besio, G., De Leo, F., Mazzino, A., 2021. Evaluation of drag coefficients under medicane conditions: Coupling waves, sea spray and surface friction. Atmospheric Research 247, 105207. URL: https://doi.org/10.1016/j.atmosres.2020.105207.

Rouse, H., 1937. Modern conceptions of the mechanics of fluid turbulence. Transactions of the American Society of Civil Engineers 102, 463–505. URL: https://doi.org/10.1061/TACEAT.0004872.

Seinfeld, J.H., Pandis, N., 1998. Atmospheric Chemistry and Physics: From Air Pollution to Climate Change. Wiley.

Skamarock, W, C., Klemp, J, B., Dudhia, J., Gill, D, O., Liu, Z., Berner, J., Huang, X, y., 2021. A Description of the Advanced Research WRF Model Version 4.3. Technical Report NCAR/TN-556+STR. NCAR Technical URL. URL: http://dx.doi.org/10.5065/1dfh-6p97.

Tedeschi, G., Piazzola, J., 2011. Development of a 2d marine aerosol transport model: Application to the influence of thermal stability in the marine atmospheric boundary layer. Atmospheric Research 101, 469–479. URL: https://doi.org/10.1016/j.atmosres.2011.04.013.

Tedeshi, G., van Eijk, A., Piazzola, J., Kusmierczyk-Michulec, J., 2017. Influence of the surf zone on the marine aerosol concentration in a coastal area. Boundary-Layer Meteorology 163, 327–350. URL: https://doi.org/10.1007/s10546-016-0229-7.

Toba, Y., 1965. On the giant sea-salt particles in the atmosphere. Tellus 17, 365–382. URL: https://doi.org/10.1111/j.2153-3490.1965.tb01429.x.

Varlas, G., Marinou, E., Gialitaki, A., Siomos, N., Tsarpalis, K., Kalivitis, N., Solomos, S., Tsekeri, A., Spyrou, C., Tsichla, M., Kampouri, A., Vervatis, V., Giannakaki, E., Amiridis, V., Mihalopoulos, N., Papadopoulos, A., Katsafados, P., 2021. Assessing sea-state effects on sea-salt aerosol modeling in the lower atmosphere using lidar and in-situ measurements. Remote Sensing 13. URL: https://doi.org/10.3390/rs13040614.

Veron, F., 2015. Ocean spray. Annual Review of Fluid Mechanics 47, 507–538. URL: https://doi.org/10.1146/annurev-fluid-010814-014651.

Vignati, E., de Leeuw, G., Berkowicz, R., 1998. Aerosol transport in the coastal environment and effects on extinction, in: Bissonnette, L.R. (Ed.), Propagation and Imaging through the Atmosphere II, International Society for Optics and Photonics. SPIE. pp. 21–30. URL: https://doi.org/10.1117/12.330223.

Vignati, E., de Leeuw, G., Berkowicz, R., 2001. Modeling coastal aerosol transport and effects of surf-produced aerosols on processes in the marine atmospheric boundary layer. Journal of Geophysical Research: Atmospheres 106, 20225–20238. URL: https://doi.org/10.1029/2000JD000025.

Wyngaard, J.C., 2004. Toward Numerical Modeling in the "Terra Incognita". Journal of the Atmospheric Sciences 61, 1816–1826. URL: https://journals.ametsoc.org/view/journals/atsc/61/14/1520-0469_2004_061_1816_tnmitt_2.0.co_2.xml, doi:10.1175/1520-0469(2004)061<1816:TNMITT>2.0.CO;2.

Xue, M., Droegemeier, K, K., Wong, W., 2000. The advanced regional prediction system (arps) - a mutli-scale nonhydrostatic atmospheric simulation and prediction model. part i: Model dynamics and verification. Meterology and Atmospheric Physics 75, 161–193. URL: https://doi.org/10.1007/s007030070003.

Yoon, Y.J., Ceburnis, D., Cavalli, F., Jourdan, O., Putaud, J.P., Facchini, M.C., Decesari, S., Fuzzi, S., Sellegri, K., Jennings, S.G., O'Dowd, C.D., 2007. Seasonal characteristics of the physicochemical properties of north atlantic marine atmospheric aerosols. Journal of Geophysical Research: Atmospheres 112. URL: https://doi.org/10.1029/2005JD007044.